

Birth and Evolution of Fast Radio Bursts: Strong Population-Based Evidence for a Neutron-Star Origin

Yuyang Wang (王宇阳)^{1,*} and Joeri van Leeuwen^{2,*}

¹ Anton Pannekoek Institute for Astronomy, University of Amsterdam, Science Park 904, 1098 XH Amsterdam, The Netherlands

² ASTRON, the Netherlands Institute for Radio Astronomy, Oude Hoogeveensedijk 4, 7991 PD, Dwingeloo, The Netherlands

May 2024

ABSTRACT

While the appeal of their extraordinary radio luminosity to our curiosity is undiminished, the nature of fast radio bursts (FRBs) has remained unclear. The challenge has been due in part to small sample sizes and limited understanding of telescope selection effects. We here present the first inclusion of the entire set of one-off FRBs from CHIME/FRB Catalog 1 in `frbpoppy`. Where previous work had to curate this data set, and fit for few model parameters, we have developed full multi-dimensional Markov chain Monte Carlo (MCMC) capabilities for `frbpoppy` – the comprehensive, open-science FRB population synthesis code – that allow us to include all one-off CHIME bursts. Through the combination of these two advances we now find the best description of the real, underlying FRB population, with higher confidence than before. We show that $4 \pm 3 \times 10^3$ one-off FRBs go off every second between Earth and $z=1$; and we provide a mock catalog based on our best model, for straight-forward inclusion in other studies. We investigate CHIME side-lobe detection fractions, and FRB luminosity characteristics, to show that some bright, local FRBs are still being missed. We find strong evidence that FRB birth rates evolve with the star formation rate of the Universe, even with a hint of a short (0.1–1 Gyr) delay time. The preferred contribution of the hosts to the FRB dispersion agrees with a progenitor birth location in the host disk. This population-based evidence solidly aligns with magnetar-like burst sources, and we conclude FRBs are emitted by neutron stars.

Key words. radio continuum: general; relativistic processes; stars: neutron; stars: magnetars; methods: statistical

1. Introduction

Fast radio bursts (FRBs) are millisecond-duration phenomena visible in the radio band. Their origin is extragalactic, implying very high energies are involved (see, e.g., Cordes & Charterjee 2019; Petroff et al. 2019, 2022, for reviews). After a first specimen was discovered in 2007 using single-pulse searches of archival Parkes telescope data (Lorimer et al. 2007), the bursts were not proven beyond a doubt to an astrophysical phenomenon (see Burke-Spolaor et al. 2010; Petroff et al. 2015, for similar human-generated signals) until four more events were found in the next decade (Thornton et al. 2013). However, their physical origins are still unclear after a further decade of studies. In general, FRBs are now empirically divided into two categories, one-offs and repeaters, depending on whether the burst are observed to recur or not. However, whether these two populations are intrinsically or physically different is still an open question. Furthermore, the periodic activity in some repeaters and host galaxy localizations for both classes are interesting for investigating their nature (see Petroff et al. 2022, and references therein), while their use for studying the intergalactic medium is also promising (e.g., Pastor-Marazuela et al. 2021).

In the early days of FRB discovery, opportunities for more quantitative studies of the FRB population were limited. This is changing: since the Canadian Hydrogen Intensity Mapping Experiment (CHIME/FRB; CHIME/FRB Collaboration et al. 2019) found 13 FRBs during its pre-commissioning runs, the ability to detect $O(1)$ to $O(10)$ FRBs per sky per day has made statistical studies of the FRB population feasible. The more than 500

FRBs contained in CHIME/FRB Catalog 1 (CHIME/FRB Collaboration et al. 2021) have been the subject of several initial population studies (e.g., Chawla et al. 2022; Shin et al. 2023; Bhattacharyya et al. 2023).

Population synthesis provides a method to study the intrinsic properties of an astronomical class, by treating the various observational biases encountered, which are hard to remove analytically. Such studies have previously been carried out in a field akin to FRBs, for understanding neutron stars (e.g. Taylor & Manchester 1977; van Leeuwen & Stappers 2010; Bates et al. 2014). In FRB detection and interpretation, coupling between the intrinsic characteristics of the sources and of the detecting instrument introduces similar, possibly strong biases (see, e.g., Connor 2019). `frbpoppy`¹ is an open source python package for population synthesis of FRBs (Gardenier 2019). It simulates the intrinsic, cosmic, underlying, parent populations and applies simulated surveys to these sources, to obtain the surveyed, detected, observed populations (as further detailed in Sect. 2.2; see Gardenier et al. 2019 for a full and in-depth discussion of these terms). Then these simulated observed populations are compared with the real observed populations by the actual telescopes. So far, the latest released version is `frbpoppy` 2.1, which includes modelling of both one-off and repeater FRBs, and options for Monte Carlo (MC) simulations. Results from studying the population of repeating FRBs using `frbpoppy` are presented in Gardenier et al. (2021). There, the authors show that a single source population of repeating FRBs, with some minor correlations of behaviour with repetition rate, can describe all CHIME/FRB observations. Subsequently, Gardenier & van Leeuwen (2021,

* y.wang3@uva.nl, leeuwen@astron.nl

¹ <https://github.com/TRASAL/frbpoppy>

hereafter: GL21) conducted a multi-dimensional MC simulation, and found a population that optimally reproduced the FRBs detected by the four largest surveys at that time (Parkes-HTRU, CHIME/FRB, ASKAP-Incoherent and WSRT-Apertif; see, e.g., Shannon et al. 2018; van Leeuwen et al. 2023). Such a multi-survey simulation has the benefit that uncertainties in the individual selection biases possibly average out; but it comes with the downsides that the overall results are harder to interpret and adjust. Since then, a different, complementary approach has become possible: with CHIME/FRB Catalog 1 (CHIME/FRB Collaboration et al. 2021) the sample size has increased from ~ 100 FRBs to many hundreds, all subjected to, in principle, the same survey biases (Amiri et al. 2022). This allows for a more straightforward population synthesis with `frbpoppy`. In this work, we include the bursts classified as one-off FRB in that catalog in `frbpoppy`.

The paper is organized as follows. In Sect. 2 we introduce the catalog, and characteristics of the FRBs contained therein; we also discuss the CHIME/FRB beam model reproduction that is essential for our simulations and describe the modeling of the intrinsic population. In Sect. 3, we introduce the methods of our new Markov chain Monte Carlo (MCMC) simulations and in Sect. 4 we present the best-fitting parameters from different models. In Sect. 5, we discuss how these compare against other studies, we outline how our data and models can be used by others, we present the implications for the FRB source population, and we describe future work. Sect. 6 describes easy access to data and code.

2. The input: catalog, populations, telescope model

2.1. The CHIME/FRB Catalog 1

CHIME is a transit radio telescope operating across the 400–800 MHz band. It is an excellent FRB detector, owing to its large field of view, wide bandwidth, and high sensitivity, plus its powerful correlator (CHIME/FRB Collaboration et al. 2018). During pre-commissioning, it detected 13 new FRBs (CHIME/FRB Collaboration et al. 2019). The CHIME/FRB Catalog 1 was next published in June 2021 (CHIME/FRB Collaboration et al. 2021), containing 536 FRBs, of which 474 are one-off bursts and 63 are bursts from 18 repeating sources. The catalog spans observing dates from 2018 July 25 to 2019 July 1². In the current work, we start by limiting ourselves to first reproducing the bursts that are classified as one-off FRBs. Note that `frbpoppy` is capable of simulating repeating FRBs too (Gardenier et al. 2021), and we will pursue that study in future work. The catalog is the first set numbering over 100 FRBs from a single telescope. That is important because such a set is governed by uniform selection effects. These selection effects determine, in large part, the overall parameter distributions that describe the observed sample – of, for example, the dispersion measures (DMs), distances, bandedness, and pulse widths. Figures 1 and 2 show how CHIME/FRB and other telescopes observe parameter distributions – i.e., how each find different kinds of FRBs. We see there that the DM distribution for the CHIME/FRB bursts is similar to that of FRBs found by other telescopes. That may initially be surprising because CHIME/FRB operates at a lower frequency than most other surveys, which would generally make higher-DM sources especially hard to find, given their low-frequency dispersion and scatter broadening. This disadvan-

² In `frbpoppy` the catalog is obtained from the Transient Name Server (TNS), through a query on these dates.

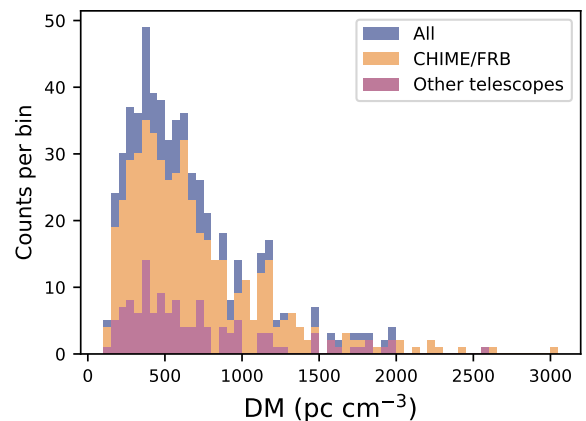


Fig. 1. The DM distribution histogram of one-off FRBs in the TNS database. The total sample of FRBs is shown in blue while those from CHIME/FRB and other telescopes are shown in orange and green respectively.

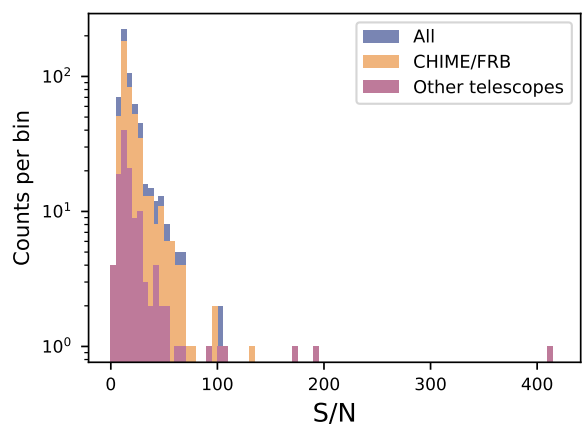


Fig. 2. The S/N distribution histogram of one-off FRBs, using the same labels and colors as Fig. 1.

tage is either overcome by the CHIME/FRB system, or it is leveled out by biases that work against low-DM sources. Indeed the latter seems to be the case, as Merryfield et al. (2023) recently found that the CHIME/FRB pipeline selects against bright, low-DM FRBs. We investigate this in Sect. 5.3. For the signal-to-noise ratio (S/N), the CHIME/FRB distribution is shifted towards higher values than that of the other telescopes.

2.2. Modelling underlying populations

As the number of detected FRBs increases, a number of sources have shown complex behaviour or circumstances. Our goal is to distill the most important trends from the complicated real FRB population. We thus use a number of parameters to model its main characteristics, both source-related properties (luminosity, pulse width) as well as population-related properties (number density, DM). Here, we describe the parameter distribution models adopted in our simulations (see Gardenier et al. 2019 for further details on these methods).

2.2.1. Number density from power-law model

To establish the number-redshift relation dN/dz of intrinsic FRB populations per comoving volume in our simulation, we adopt a power-law (PL³) model by modifying the uniform sampling $U(0, 1)$ with exponent β

$$V_{\text{co,FRB}} = V_{\text{co,max}} \cdot U(0, 1)^\beta, \quad (1)$$

where β determines the slope of the cumulative source-count distribution for detected FRBs, above a certain peak flux density detection threshold, at the high flux density end. The parameter α is introduced via

$$\alpha = -\frac{3}{2\beta}. \quad (2)$$

In a Euclidean universe, where the FRB count per comoving volume element does not evolve with redshift, we have $\beta = 1$ and $\alpha = -3/2$. Although α is introduced via the PL index, it is the same as the $\log N$ - $\log S$ slope in the high fluence limit.

2.2.2. Number density from star formation rate model

There is ongoing discussion on whether the FRB event rate tracks the cosmic star formation rate (SFR). James et al. (2022b) find it does. Zhang et al. (2021) and Zhang & Zhang (2022), however, claim that the FRB population as a whole does not track the SFR; while a delayed SFR model, potentially caused by compact binary mergers, cannot be rejected with the ASKAP and Parkes sample. So, in this work, we consider both the SFR itself, plus delayed SFR models with three different delay times: 0.1, 0.5, and 1 Gyr. Note that for this delay-time distribution, we use a constant delayed time model (where Zhang et al. 2021 mention various other distributions). We discuss the results in Sect. 4.1.2 and Sect. 4.1.3.

2.2.3. Spectral index

The spectral index si describes the relative flux density at different frequencies within the spectrum. In frbpoppy, this index acts through converting the FRB fluence into the observing bands of the modeled surveys (see Eq. 8 describing S_{peak}). It is arguably best constrained by comparing FRB fluences and rates from survey at different frequencies. Such multi-survey simulations are one of the strong points of frbpoppy and we will explore this aspect in future work. In the current work, however, we only model CHIME/FRB, effectively at a single frequency band. In this case the resulting si is greatly influenced by the choice of ν_{low} , ν_{high} , and the assumption that the power-law relationship ($E_\nu \propto \nu^\gamma$) holds throughout the whole frequency range. As this degeneracy cannot be solved in a single-frequency study, we do not treat si as a free parameter in the current work, but set it to -1.5 , a commonly adopted value found by Macquart et al. (2019) using a sample of 23 FRBs detected with ASKAP.

2.2.4. Luminosity

The bolometric luminosity L_{bol} is generated from a power-law distribution with power-law index li and range $[L_{\text{min}}, L_{\text{max}}]$. Since the publication of Gardenier & van Leeuwen (2021), the detection of FRB 20220610A has raised the maximum observed

³ To prevent confusion with with the *luminosity* distribution that is also drawn from a power law, we only use the acronym PL for the *number density* model.

rest-frame burst luminosity to 10^{46} erg s⁻¹ (Ryder et al. 2023), so we have increased L_{max} to the same value. Inferred luminosities depend on the assumed bandwidth of emission; so some caution is required when comparing these numbers. To provide context to this extreme luminosity we note that the magnetic Eddington limit of a strong-field ($> 3 \times 10^{14}$ G) neutron star is 10^{42} erg s⁻¹ (Thompson & Duncan 1995). Whether a lower limit to the one-off FRB luminosity exists is unclear. The $\sim 10^{37}$ erg s⁻¹ luminosity of nearby repeating FRB 20200120E (Bhardwaj et al. 2021) already indicates the underlying process, if the same, can operate over a range of brightness. To limit computing time our simulations require a lower bound though, and for the one-off FRBs under consideration here, we choose $L_{\text{min}} = 10^{41}$ erg s⁻¹. This is 3 orders of magnitude below the least luminous localised one-off bursts, such as FRB 190608 (Macquart et al. 2020) at $\sim 10^{44}$ erg s⁻¹ (although given the current state-of-the-art, only relatively bright FRBs can generally be localised). As it is also conservative compared to the $L_{\text{min}} = 7 \times 10^{42}$ erg s⁻¹ suggested by Cui et al. (2022) for their CHIME/FRB non-repeater sample, we are confident our simulation coverage is complete.

2.2.5. Pulse width

The intrinsic pulse width w_{int} is modeled with a log-normal distribution

$$p(x) = \frac{1}{x} \cdot \frac{1}{\sigma \sqrt{2\pi}} \exp\left(-\frac{(\ln x - \mu)^2}{2\sigma^2}\right), \quad (3)$$

where μ , σ are related to the input parameters $w_{\text{int, mean}}$ and $w_{\text{int, std}}$ by $w_{\text{int, mean}} = \exp(\mu + \sigma^2/2)$ and $w_{\text{int, std}} = \sqrt{[\exp(\sigma^2) - 1] \exp(2\mu + \sigma^2)}$.

The pulse width w_{arr} of an FRB arriving at Earth is

$$w_{\text{arr}} = (1 + z) w_{\text{int}}. \quad (4)$$

The observed pulse width is

$$w_{\text{eff}} = \sqrt{w_{\text{arr}}^2 + t_{\text{scat}}^2 + t_{\text{DM}}^2 + t_{\text{samp}}^2}. \quad (5)$$

where t_{scat} is the scattering time while t_{samp} and t_{DM} are the result of instrumental broadening. In our simulation, a log-normal distribution for t_{scat} is adopted (see Fig. 14, right panel); t_{samp} is 0.98304 ms as in CHIME/FRB Catalog 1; and t_{DM} is the intra-channel dispersion smearing the CHIME/FRB back-end incurs for each FRB.

2.2.6. Dispersion measure

The total DM of an FRB is

$$\text{DM}_{\text{total}} = \frac{\text{DM}_{\text{host}}}{1 + z} + \text{DM}_{\text{IGM}} + \text{DM}_{\text{MW}}, \quad (6)$$

where DM_{host} is the host galaxy contribution (including the circumburst environment contribution DM_{src} and Milky Way halo contribution $\text{DM}_{\text{MW,halo}}$) in the source rest frame. We generate DM_{host} using a log-normal distribution ($\ln \text{DM}_{\text{host}} \sim N(\sigma, \mu)$), where input parameters $\text{DM}_{\text{host, mean}}$ and $\text{DM}_{\text{host, std}}$ represent the mean and standard deviation of the log-normal distribution respectively; DM_{MW} is the Milky-Way interstellar medium (ISM) contribution obtained from the NE2001 model (Cordes & Lazio 2002).

The intergalactic medium (IGM) contribution DM_{IGM} is estimated using a linear relation with redshift $\text{DM}_{\text{IGM}} \approx$

$DM_{\text{IGM,slope } z}$ (Zhang 2018; Macquart et al. 2020), around which we include the spread from a normal distribution, leading to

$$DM_{\text{IGM}} = N\left(DM_{\text{IGM,slope } z}, 0.2 DM_{\text{IGM,slope } z}\right). \quad (7)$$

As the value of $DM_{\text{IGM,slope } z}$ derived in Macquart et al. (2020, their Fig. 2) is $\sim 1000 \text{ pc cm}^{-3}$, and the lower limit on their 90%-confidence interval is $\sim 700 \text{ pc cm}^{-3}$, we set the lower limit in our MCMC parameter search space to be 600 pc cm^{-3} .

We discuss a number of implications from our simulation for the DM_{IGM} model in Sect. 5.

2.3. The CHIME/FRB detection system model

Using `frbpoppy`, we first generate simulated intrinsic populations according to certain parameter distribution models. We then set up "surveys" with survey parameters for specific telescopes. We apply each survey to each intrinsic population, selecting the events that meet the S/N threshold to form detected populations. We compare the simulated detected populations to the actually detected population. From the best match, we infer the actual intrinsic population (as in Gardenier et al. 2019).

2.3.1. The beam model

An initial approximation of the CHIME primary beam was previously included in `frbpoppy` (Gardenier et al. 2021). There it consisted of a North-South cosine function convolved with an East-West Airy disk pattern. The behavior of the synthesized beams formed in subsequent stages is more straightforward, and well known. Since then, a CHIME primary-beam pattern measurement was empirically derived from the telescope response to the Sun (Amiri et al. 2022). Using the accompanying `cfbm` package⁴, we now include this improved CHIME/FRB beam intensity at 600 MHz in `frbpoppy`. The implemented beam model is shown in Fig. 3, left panel, with the East-West slice ($y=0^\circ$) and North-South slice along the meridian ($x=0^\circ$) shown in upper right and bottom right panels respectively.

Although only three one-off FRBs are detected outside the main beam ($|\text{East-West offset}| > 2.0^\circ$) in CHIME/FRB Catalog 1, this side-lobe detection fraction is important to distinguish models with different redshift distributions and luminosity models. The main-lobe and side-lobes arguably deliver both a deep and a shallow survey. Therefore, we will not restrict ourselves to the main beam but we consider the East-West range of $[-15^\circ, 15^\circ]$. We end before the significant drop in intensity beyond that range. These borders are indicated with dash-dotted lines in Fig. 3. Although the far side-lobe of the CHIME/FRB beam is yet poorly understood (CHIME/FRB Collaboration et al. 2021) and the three side-lobe events (FRB 20190210D, FRB 20190125B, and FRB 20190202B) are excluded in many statistical studies, they are included in our simulations, as we expect them to put significant constraints on the number density models, luminosity distributions and high S/N events.

2.3.2. Modelling CHIME surveying

In the surveying step, the S/N of an FRB is derived from its peak flux density \bar{S}_{peak} and pulse width. This peak flux density

⁴ <https://github.com/chime-frb-open-data/chime-frb-beam-model>

(Lorimer et al. 2013; Gardenier et al. 2019) is

$$\bar{S}_{\text{peak}} = \frac{L_{\text{bol}}(1+z)^{\gamma-1}}{4\pi D(z)^2} \left(\frac{v_2^{\gamma+1} - v_1^{\gamma+1}}{v_2 - v_1} \right) \left(\frac{w_{\text{arr}}}{w_{\text{eff}}} \right), \quad (8)$$

where $v'_{\text{high}} = 10 \text{ GHz}$, and $v'_{\text{low}} = 100 \text{ MHz}$, $v_2 = 800 \text{ MHz}$ and $v_1 = 400 \text{ MHz}$ are adopted; γ notates the spectral index si ; $D(z) = d_L(z)/(1+z)$ is the proper distance of the source; and the luminosity distance $d_L(z)$ is calculated with

$$d_L(z) = \frac{c(1+z)}{H_0} \int_0^z \frac{dz}{\sqrt{\Omega_m(1+z)^3 + \Omega_\Lambda}}, \quad (9)$$

where we use Planck15 results $H_0 = 67.74 \text{ km s}^{-1} \text{ Mpc}^{-1}$, $\Omega_m = 0.3089$ and $\Omega_\Lambda = 0.6911$ for a flat Lambda cold dark matter (Λ CDM) universe (Planck Collaboration et al. 2016)⁵. The S/N is derived using

$$S/N = I \frac{\bar{S}_{\text{peak}} G}{\beta T_{\text{sys}}} \sqrt{n_{\text{pol}} (v_2 - v_1) w_{\text{eff}}}, \quad (10)$$

where I is the beam intensity at the detection location, G is the gain, β is the degradation factor, T_{sys} is the total system temperature specific to CHIME/FRB, n_{pol} is the number of polarizations, and $v_{1,2}$ are the boundary frequencies of the survey, respectively (Lorimer & Kramer 2004). For the CHIME/FRB gain, degradation factor and total system temperature we update the preliminary numbers used in Gardenier et al. (2021) and follow Merryfield et al. (2023). The measured system equivalent flux density (SEFD) reported there ranges from 30 to 80 Jy over the band. Merryfield et al. (2023) initially used a value of 45 Jy in their injection system but found their idealized assumptions did not represent the system adequately; requiring an increase of the injection threshold from 9σ to 20σ . We here aim to include this real-life factor of 2 over the theoretical performance for an SEFD of 45 Jy by using the average SEFD reported over the band (55 Jy, implemented as gain $G = 1 \text{ K Jy}^{-1}$ and $T_{\text{sys}} = 55 \text{ K}$) and a degradation factor β of 1.6. We discuss the influence of these updated numbers in Sect. 5.4.

Up to and including `frbpoppy` 2.1 the S/N formula, Eq. 10, erroneously used w_{arr} (Eq. 17 in Gardenier et al. 2019), not w_{eff} , for the observed pulse width. This meant that while \bar{S}_{peak} was correctly decreased by the factor $w_{\text{arr}}/w_{\text{eff}}$ in Eq. 8, the accompanying, partly counterbalancing increase in S/N by $\sqrt{w_{\text{eff}}}$ in Eq. 10 was not properly accounted for. This made smeared-out pulses harder to detect than in real life. That is corrected in `frbpoppy` 2.2 and in our results below. The impact of this change is, for example, that higher-DM FRBs are slightly easier to detect, influencing α . To determine the impact of the change, we compare the best-fit PL models against it, and find that the values describing the underlying population (Table 1) changed by about $0-0.4\sigma$.

2.3.3. Comparisons with the CHIME/FRB injection system

Part of our approach is similar, in goals and method, to the CHIME/FRB injection system mentioned above (Merryfield

⁵ The Hubble tension (Riess et al. 2022; Hu & Wang 2023) between the local distance indicator and the cosmic microwave background (CMB) can result in up to 10% discrepancy in distances and the inferred redshifts from DM_{IGM} . The impact of this uncertainty will not be investigated in this work.

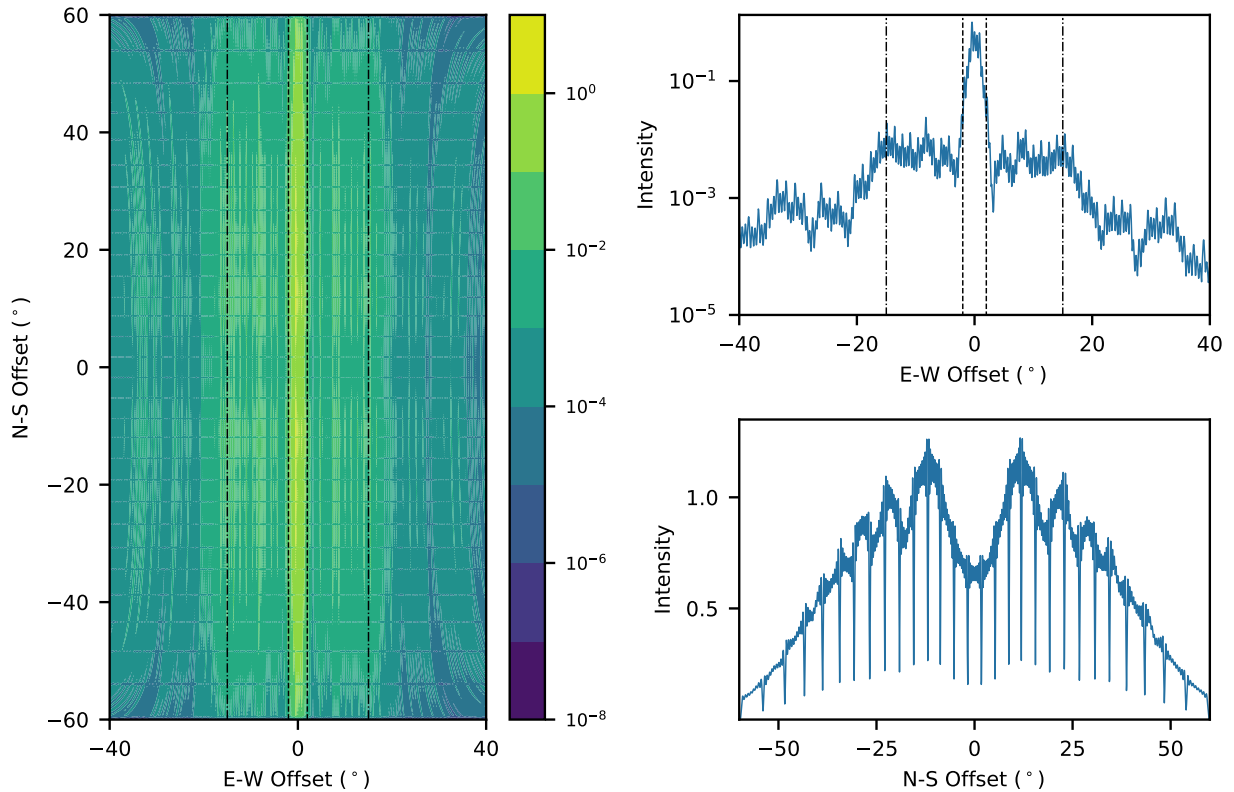


Fig. 3. The CHIME/FRB beam model reproduced with `cfbm` at 600 MHz. The left panel shows the beam intensity map in the range $[-40^\circ, 40^\circ]$ (East-West) and $[-60^\circ, 60^\circ]$ (North-South). The upper and bottom right panels show the East-West slice ($y=0^\circ$) and North-South slice along the meridian ($x=0^\circ$) respectively. The relative beam intensity is dimensionless, and normalized to the transit of Cyg A (Amiri et al. 2022). To include the side-lobe in our simulation, the beam range $[-15^\circ, 15^\circ]$ (East-West) \times $[-60^\circ, 60^\circ]$ (North-South) is considered, where the East-West borders are indicated with dash-dotted lines.

et al. 2023). There, a mock population of synthetic FRBs is injected into the real-time search pipeline to determine the selection functions. Our main goal with `frbpoppy` is to next go beyond this essential expression of the selection functions: we focus on determining the intrinsic population distributions, and we argue that the best way to include the relevant biases imposed by the Universe and telescope is through forward modelling.

In contrast to using the selection functions or fiducial distributions from CHIME/FRB Collaboration et al. (2021) or Merryfield et al. (2023), the flexibility of forward modelling allows us to determine which selection factors contribute most, thus leading to better understanding of the interaction between the intrinsic population and the telescope strengths and weaknesses. This is only possible if the survey is modeled in the same simulation as the population. Furthermore, certain parameters – e.g. the spectral index, the activity dependence on frequency – can only be done in a multi-survey simulation, which means one has to treat selection effects similarly for all.

3. Methods

Our aim is to find the global best-fit model for describing the FRBs emitted in the Universe, which are then input to the modeled telescope. The sample of bursts can be well described by of order 10 characteristic numbers. A fit over such a large number of parameters is, however, computationally challenging. To realise this after all, we have improved `frbpoppy` code and application in three ways. We first add MCMC sampling, we

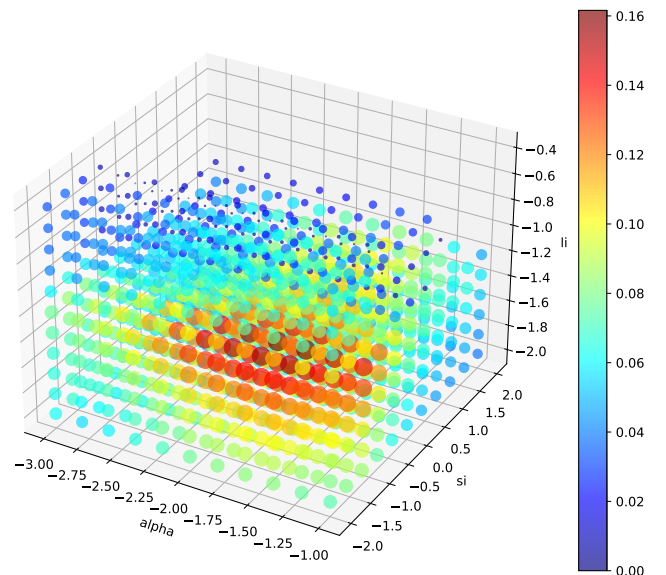


Fig. 4. The 3-dimensional GoF plot for $\{\alpha, si, li\}$ from MC simulation. Different GoFs are denoted with colors as well as marker sizes.

next employ data reuse where possible, and we finally deployed `frbpoppy` on a supercomputer. These are described below.

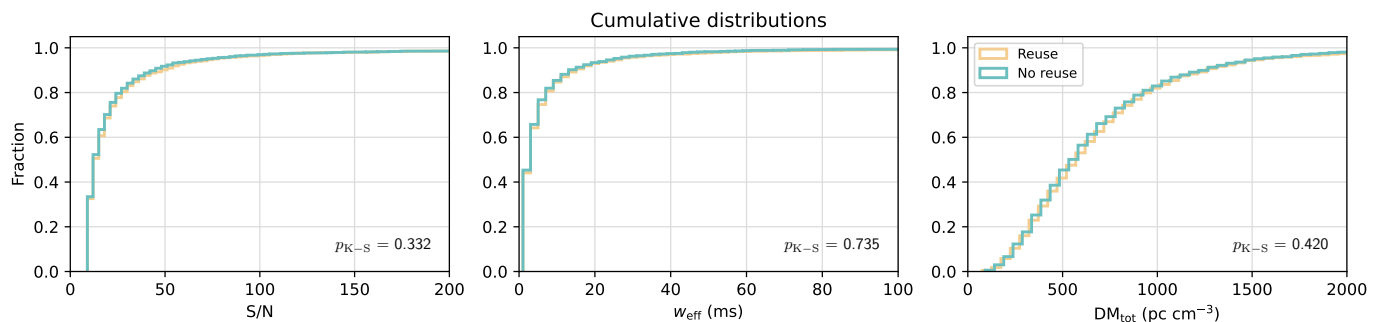


Fig. 5. The CDF plots of S/N, w_{eff} and DM_{total} distributions from two surveyed populations generated with and without reuse, for the PL model. The p -value of K-S test is also shown for reference.

3.1. Markov chain Monte Carlo

Gardenier & van Leeuwen (2021, GL21) conducted a multi-dimensional MC simulation over 9 parameters, all explained above: α , si , li , L_{min} , L_{max} , $w_{\text{int, mean}}$, $w_{\text{int, std}}$, $\text{DM}_{\text{IGM, slope}}$, and DM_{host} . Due to computational limitations, in that work these 9 parameters were divided over 4 subsets, chosen to be maximally independent of each other, but with a few shared parameters between sets, such that the globally best model could arguably be approached: 1: $\{\alpha, si, li\}$, 2: $\{li, L_{\text{min}}, L_{\text{max}}\}$, 3: $\{w_{\text{int, mean}}, w_{\text{int, std}}\}$ and 4: $\{\text{DM}_{\text{IGM, slope}}, \text{DM}_{\text{host}}\}$. Each time, one subset was searched, keeping other parameters fixed, using the best-fitting values of previous run as the input of the subsequent run. This was repeated over multiple cycles to approach the global optimum. Fig. 4 serves as an example of the 3-dimensional goodness-of-fit (GoF) plot from such an *frbpoppy* MC simulation; in this case for $\{\alpha, si, li\}$. A down side of this approach, also discussed in GL21, is that during every run the uniform sampling means regions of low and high GoF are treated equally, and searched with the same step size. Thus, the MC simulation spends a considerable amount of computing time in regions that are not actually interesting.

Therefore, we implement and conduct a full dimensional MCMC simulation⁶, to supersede the GL21 MC simulation with divided subsets. As the MCMC sampler moves out of regions of poor GoF more quickly than the brute-force method employed earlier, this allows us to sample the full multi-dimensional search space. Additionally beneficial is that such sampling allows for error estimates on the outcome values, something the previous, subset implementation lacked.

For a given set of input parameters, we first generate a small population of 10^6 FRBs, then follow these through our CHIME/FRB representation, and save the detected FRBs to the surveyed population. Note that, like in Gardenier et al. 2019, we use the terms “surveyed”, “observed” and “detected” synonymously. We repeat the process until we have enough FRBs (e.g. 1000) in the surveyed population. To limit the computational time required when sampling poor regions, we also stop if after a certain number of iterations we do not have enough detections.

GL21 use the p -value p_{K-S} from the two-sample Kolmogorov-Smirnov (K-S) test as GoF in their MC simulation, to evaluate which population is more similar to the observed population. The growing size of the observed sample, however, means the high S/N or high DM events are approaching the actual boundaries of the population. Since the models or parameters we are trying to constrain make different

predictions for these boundaries, the outlier events can be of great significance to evaluate population models. Therefore, we have extended *frbpoppy* with the option to use the k -sample Anderson-Darling (A-D) test (Scholz & Stephens 1987) as the measure to determine the GoF. The statistic A^2 of the A-D test uses weighting functions when it sums the cumulative distribution function (CDF) distances between samples, giving more weight to the tail of distributions. In maximum likelihood estimation (MLE), the log-likelihood function then is the negative of the loss function (the statistic)

$$\ln L \propto -A^2. \quad (11)$$

To represent the main features of FRB populations, we compare the S/N, w_{eff} and DM_{total} distributions from a simulation with the CHIME/FRB Catalog 1 one-off FRBs⁷. To combine these three distributions to constrain the parameter set, we use as the log-likelihood function $\ln L$ the sum of the three statistic A_i^2

$$\ln L = -A_{S/N}^2 - A_{w_{\text{eff}}}^2 - A_{\text{DM}}^2, \quad (12)$$

Here, we assume that the three distributions are uncorrelated, and that when $\ln L_{\text{max}}$ is reached, we have identified the joint minimum of $A_{S/N}^2$, $A_{w_{\text{eff}}}^2$ and A_{DM}^2 . We use $\ln L$ (i.e., $-\sum A_i^2$) as the total GoF to evaluate how well a set of parameters within the specific model reflects the simulated samples match real observations. We discuss these statistics more in Sect. 5.9.

3.2. Speeding up of *frbpoppy*

In order to feasibly operate *frbpoppy* within an MCMC, a number of code optimizations and changes were implemented, to speed up the generation of large populations. We now use numpy array look-up methods, superseding the SQL database approached used in *frbpoppy* 2.1.0 (Gardenier et al. 2019), to query the DM_{MW} and the cosmological distance d_L .

A population in *frbpoppy* contains property values for e.g., distance, luminosity, pulse width and DM. When generating a new population, *frbpoppy* now has the option to reuse some of these quantities. This is especially beneficial for values that are expensive to generate but are uncorrelated with other values. In this way, run time can be reduced by $\sim 50\%$. Under this mode, we start from a relatively small population (10^6 FRBs) for which all parameters are drawn from the selected model. In the simulated population, the redshift z , distance d_{co} , coordinates (g_l, g_b) , and dispersion measure (including DM_{host} , DM_{IGM} and

⁶ Using the python module *emcee* (Foreman-Mackey et al. 2013).

⁷ For S/N, we compare with *bonsai_snr* in CHIME/FRB Catalog 1.

DM_{MW}) are coupled. They should be reused as a whole. On the other hand, the FRB-intrinsic properties, i.e., the luminosity L_{bol} , and pulse width w_{int} are independent of this first set, and can safely be regenerate from the parent distribution. These create new FRBs that are not meaningfully correlated with those in the genesis population. All small populations thus generated are next merged to form a large population (hereafter, the combined population). This means that each set (z , d_{co} , g_l , g_b , DM_{host} , DM_{IGM} , and DM_{MW}) will be used N times in the large population, combined with different L_{bol} and w_{int} . To validate this approach, we generated surveyed populations both with and without reusing these quantities, and find they are practically identical, with similar K-S test p -values (see, e.g., Fig. 5). Fewer than 1% of FRBs will have identical coordinates and redshifts. As a further check, we compared full MCMC runs of the PL model with and without reusing quantities, and found no significant differences in the best-fitting values. Hence, the new strategy is robust and will not influence our detection of FRBs. We employ this reuse in the results discussed in the remainder of the paper.

Using these optimizations frbpoppy 2.2.0 generates a population about 20 times faster than frbpoppy 2.1.0.

3.3. Computations

The computations were carried out on the Dutch national supercomputer Snellius⁸, using the 128-core “thin” or “rome” nodes. For our default MCMC simulation of 240 nwalkers \times 500 steps, the computational cost is $2\text{--}8 \times 10^4$ core hours, depending on the FRB population models and beam intensity map.

4. Results

Below we present the outcomes of our MCMC simulations. The interpretation is covered in Sect. 5.

4.1. Best-fitting parameters from different number density models

4.1.1. Power-law number density model

The confidence contours and marginalized likelihood distributions for the power-law number density model are shown in Fig. 6 and the best-fitting values with 1σ uncertainties are listed in Table 1, for the population parameter set $\{\alpha, li, \log_{10} w_{int, mean}, w_{int, std}, DM_{IGM, slope}, DM_{host, mean}, DM_{host, std}\}$.

The number density power-law index $\alpha = -1.58^{+0.09}_{-0.27}$ is consistent with the non-evolving Euclidean distribution (Oppermann et al. 2016; James et al. 2019). The luminosity index li is constrained to $-1.51^{+0.09}_{-0.28}$; and we discuss this finding, and compare it with other results – minding the different definitions – in Sect. 5.5. For pulse width, the best-fitting values of $\log_{10}(w_{int}/ms)$ is $-0.45^{+0.15}_{-0.30}$. This produce mean intrinsic pulse widths two orders of magnitude higher than in GL21 – this difference is explained in Sect. 2.3.2.

For the components that contribute to the DM, we find the $DM_{IGM, slope}$ is 780^{+349}_{-94} pc cm⁻³ while the $DM_{host, mean}, DM_{host, std}$ are 560^{+37}_{-190} pc cm⁻³ and 610^{+176}_{-124} pc cm⁻³ respectively. We note here that the mean and standard deviation of DM_{host} describe a log-normal distribution; hence, they are quite far away from the more meaningful median value. After conversion, the median of the observed distribution for DM_{host} is ~ 330 pc cm⁻³ and its probability density function (PDF) peaks at ~ 130 pc cm⁻³ (both

in the source frame). These values are larger than what Zhang et al. (2020) found from the IllustrisTNG simulation and Yang et al. (2017) from a sample of 21 FRBs. It is worth noting that the DM_{src} and $DM_{MW, halo}$ contributions are absorbed into the DM_{host} term in the simulations. $DM_{MW, halo}$ is not explicitly modeled in NE2001 (Cordes & Lazio 2002, 2003). Prochaska & Zheng (2019) estimated $DM_{MW, halo} \sim 50 - 80$ pc cm⁻³. Yamasaki & Totani (2020) reported a mean value of $DM_{MW, halo} \sim 43$ pc cm⁻³. For simplicity, in the following discussions and in Fig. 15 in this work, we adopt a typical $DM_{MW, halo}$ of 40 pc cm⁻³ and subtract it from the reported DM_{host} results.

4.1.2. SFR model

We describe the SFR model using parameters similar to the PL model (above) but without requiring a number density power-law index α , leading to the 6-parameter set $\{li, \log_{10} w_{int, mean}, w_{int, std}, DM_{IGM, slope}, DM_{host, mean}, DM_{host, std}\}$. The confidence contours and marginalized likelihood distributions are shown in Fig. 7 while the best-fitting values with 1σ uncertainties are also listed in Table 1. The constraints on $\{li, \log_{10} w_{int, mean}, w_{int, std}\}$ are very close to those of PL model; however, noticeable differences exist in $\{DM_{IGM, slope}, DM_{host, mean}, DM_{host, std}\}$. The median of observed source frame DM_{host} is ~ 279 pc cm⁻³ and its PDF peaks at ~ 105 pc cm⁻³. This is larger than the median value 179 ± 63 pc cm⁻³ found in Mo et al. (2023) for their SFR model.

In Fig. 7, the slightly diagonal confidence contours in the subpanels that project $DM_{IGM, slope}$ against the DM_{host} parameters indicate that the DM contributions of the IGM and the host are somewhat degenerate with each other. This is because the DM excess ($DM_{total} - DM_{MW}$) is supplied by the combination of $DM_{IGM, slope} z$ and $DM_{host}/(1+z)$. Models that produce fewer local FRBs, like the SFR model, will thus require a larger $DM_{IGM, slope}$ and a smaller DM_{host} to fit the observed distributions, compared to the PL model.

4.1.3. Delayed SFR model

To investigate the impact of formation channels that are delayed with respects to the SFR, we simulate three models with a different mean delay time, of 0.1 Gyr, 0.5 Gyr and 1 Gyr. In these models, the number of present-day, local FRBs is determined by the SFR when the delay process commenced. As the recent SFR declines steeply (see e.g. Gardenier et al. 2021), the number of local FRBs is expected to increase with longer delay times. FRBs with a mean delay time of 1 Gyr were formed near $z \approx 0.1$, where the SFR was $\sim 30\%$ higher. Thus, models with longer delay times in principle contain more low- z FRBs; or, reciprocally, such models require a lower source density to produce the number of FRBs that are observed. As the simulated detection numbers in frbpoppy are scaled to the actually detected number, we cannot easily identify an overall increase in the number of local FRB sources. The GoF would only be affected if there was a significant change in *slope* within the sampled redshift range. This effect is visible in the zoomed-in plot in the right panel of Fig. 8, where the shapes of the three SFR models resemble one another very closely. These are normalised to the same number of detections; the differences only emerge in the underlying physical rate. The posterior probability distributions are shown in Fig. 9. As all four SFR models have very similar best-fitting values, we cannot confidently distinguish between these. We thus corroborate the conclusion from Shin et al. (2023) that there is insufficient evidence in CHIME/FRB Catalog 1 to strongly con-

⁸ <https://www.surf.nl/en/dutch-national-supercomputer-snellius>

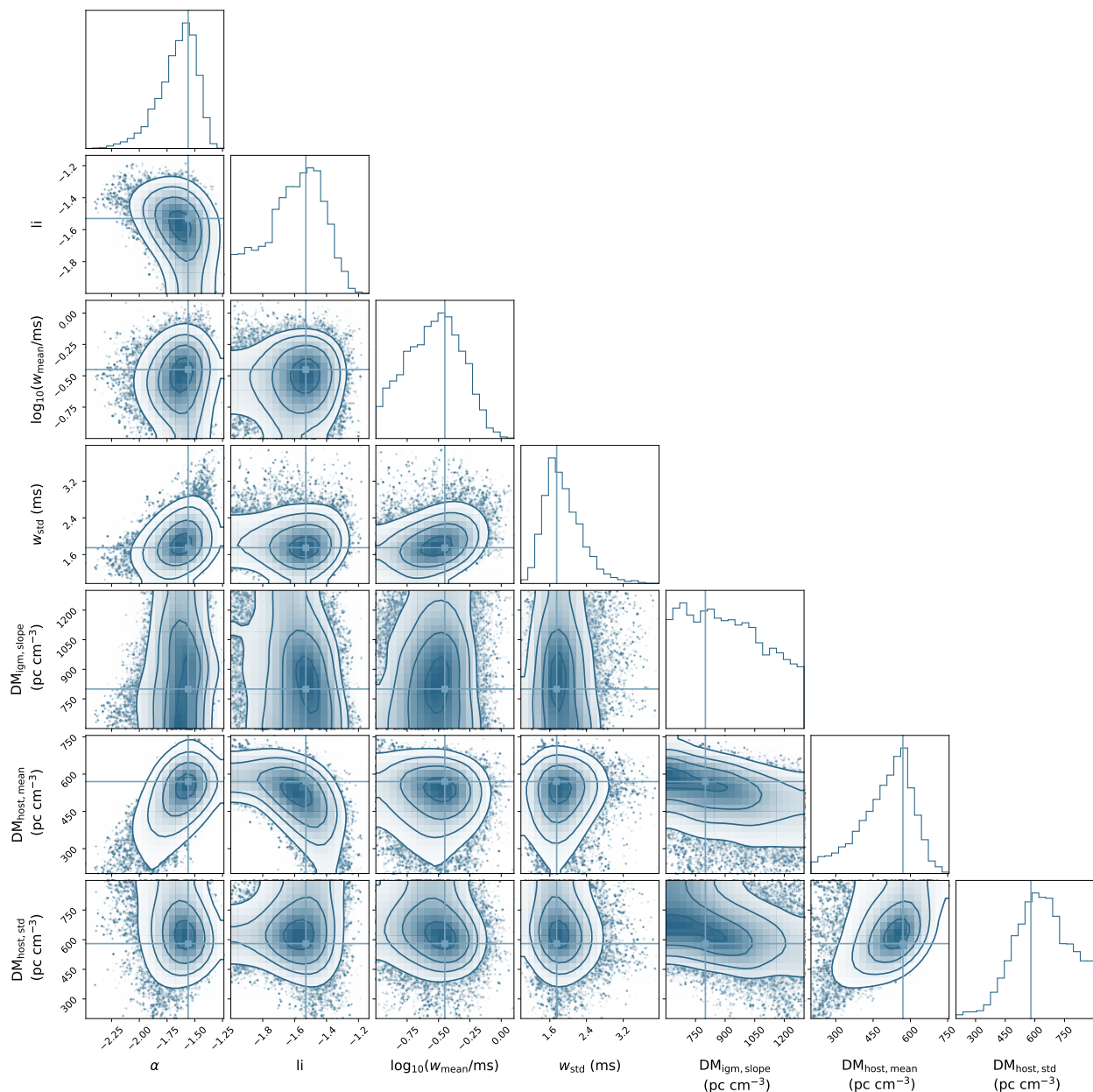


Fig. 6. Confidence contours and marginalized likelihood distributions for the 7 parameters in our PL number density model.

strain how FRB evolution follows the SFR. There is, however, so-called strong evidence (Raftery 1995) in the Bayesian Information Criterion (BIC) in favor of the SFR models over the PL model (Table 2). This conclusion differs from Zhang & Zhang (2022), who prefer a significant lag: a log-normal delay model with a central value of 10 Gyr and a standard deviation of 0.8 dex.

4.2. Reproducing CHIME/FRB distribution and model comparison

With the best-fitting values from the MCMC, we reproduce the FRB populations and surveyed them with our model of CHIME/FRB. The CDF of S/N, w and DM_{total} are shown in Fig. 10. The CHIME/FRB Catalog 1 distributions are also shown for comparison. The CDF curves of w_{eff} show good agreements with CHIME/FRB while those of S/N has the largest discrepancy for all models. The overall good reproduction of all three

distributions supports the method that we sum the A-D statistics to construct the log likelihood function.

To compare the models, we use the BIC (mentioned above):

$$\text{BIC} = k \ln n - 2 \ln L_{\text{max}} \quad (13)$$

where k is the number of free parameters in the model, n is the number of samples. In the PL model, $k = 7$; in the SFR and delayed SFR models, $k = 6$. A summary of the A-D statistic and BIC for different models is provided in Table 2. Raftery (1995) list that BIC differences between 0–2, 2–6, and 6–10 correspond to "weak", "positive" and "strong" evidence respectively. To avoid over-interpretation we refer to BIC differences between 0–2 as only a hint of evidence. Therefore, the three delayed SFR models, with almost the same BICs, show a hint of evidence over the SFR model; and all four are strongly favored over the PL model. The PL model produces the least favorable fit, especially in the S/N distribution.

Parameters	α	li	$\log_{10}(w_{\text{int, mean}}/\text{ms})$	$w_{\text{int, std}}$	$DM_{\text{IGM, slope}}$	DM_{host}	$DM_{\text{host, mean}}$	$DM_{\text{host, std}}$
Models				ms	pc cm^{-3}	pc cm^{-3}	pc cm^{-3}	pc cm^{-3}
GL21	-2.2	-0.8	-2.44	0.6	1000	50	-	-
This work:								
PL	$-1.58^{+0.09}_{-0.27}$	$-1.51^{+0.09}_{-0.28}$	$-0.45^{+0.15}_{-0.30}$	$1.75^{+0.55}_{-0.26}$	780^{+349}_{-94}	-	560^{+37}_{-190}	610^{+176}_{-124}
SFR	-	$-1.58^{+0.10}_{-0.18}$	$-0.50^{+0.22}_{-0.19}$	$1.65^{+0.40}_{-0.28}$	840^{+303}_{-140}	-	490^{+74}_{-129}	520^{+209}_{-134}
Delayed SFR - 0.1 Gyr	-	$-1.64^{+0.11}_{-0.23}$	$-0.52^{+0.17}_{-0.28}$	$1.70^{+0.31}_{-0.27}$	790^{+353}_{-104}	-	510^{+78}_{-103}	540^{+189}_{-111}
Delayed SFR - 0.5 Gyr	-	$-1.62^{+0.10}_{-0.25}$	$-0.53^{+0.19}_{-0.27}$	$1.68^{+0.35}_{-0.25}$	800^{+352}_{-100}	-	510^{+68}_{-115}	550^{+178}_{-121}
Delayed SFR - 1 Gyr	-	$-1.65^{+0.13}_{-0.22}$	$-0.54^{+0.20}_{-0.28}$	$1.68^{+0.33}_{-0.31}$	840^{+303}_{-140}	-	510^{+76}_{-111}	560^{+169}_{-131}

Table 1. The best-fitting values of the population parameters, plus and minus the 1σ uncertainty, from the MC simulation in GL21, compared to the MCMC simulations of PL, SFR and three delayed SFR models presented in this work. For formatting unity, insignificant digits are also included in certain values and errors.

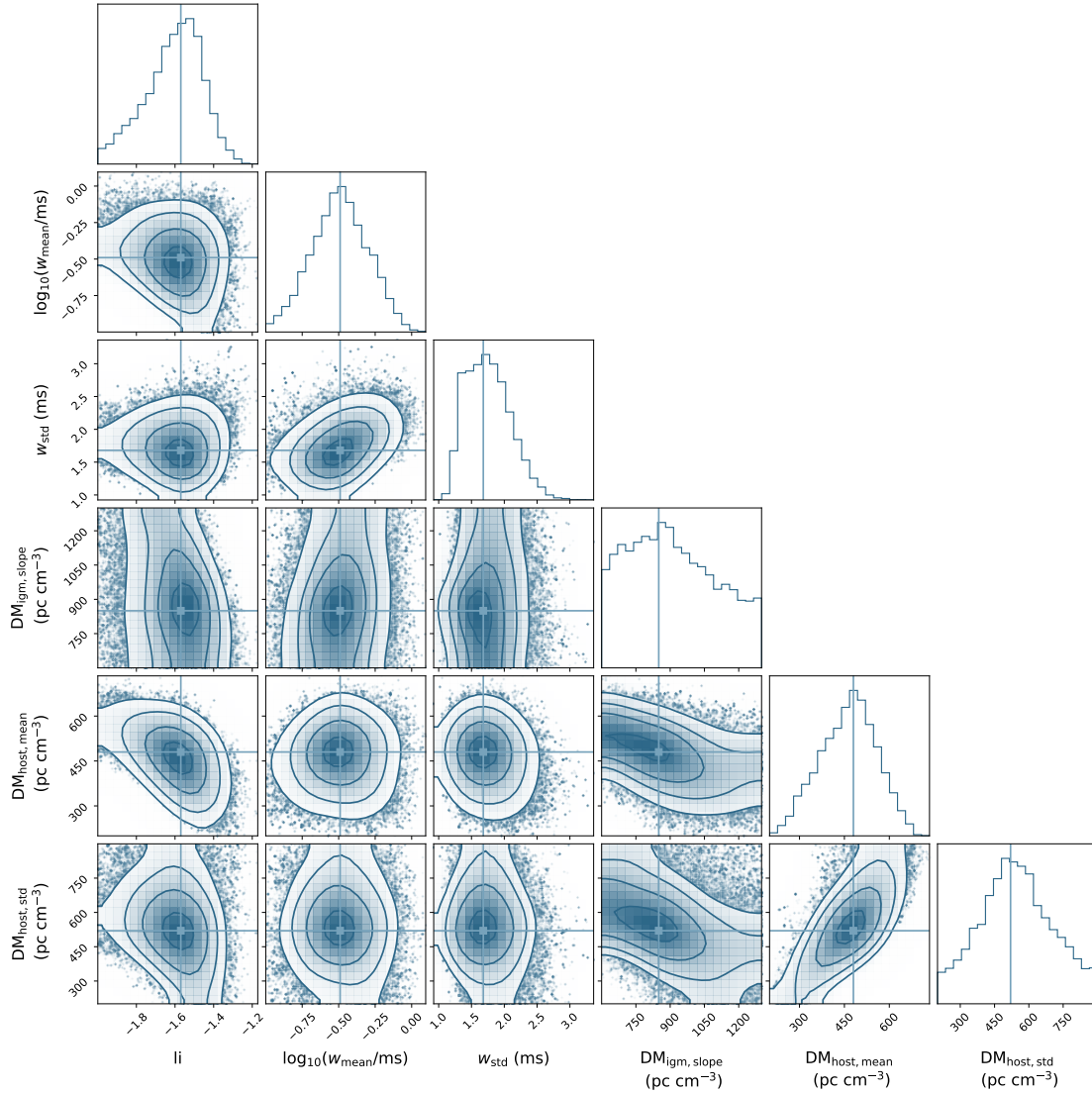


Fig. 7. The confidence contours and marginalized likelihood distributions for the 6 parameters in our SFR model.

5. Discussion

Our results provide new insights into how many FRBs are born in our local universe and their evolution, into the brightness and emission of the bursts, and into the baryonic material between the emitters and Earth. These warrant discussion and interpreta-

tion. We provide this below, ordered from more general to more expert topics.

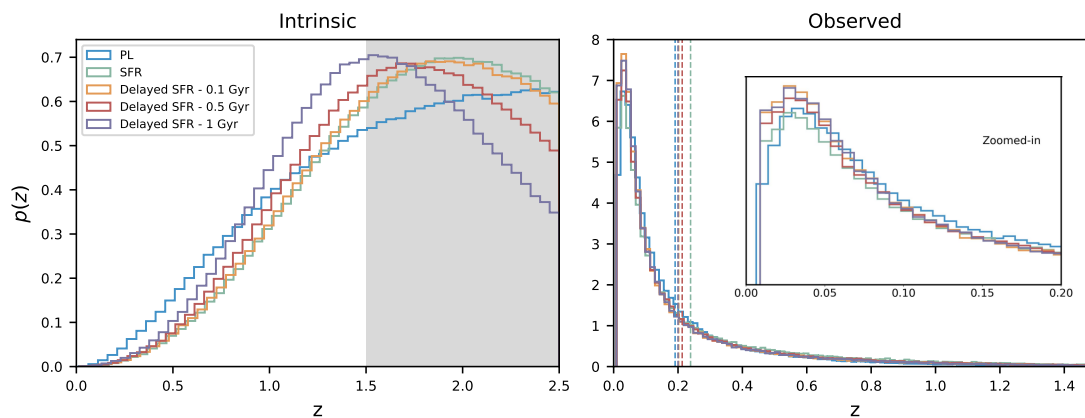


Fig. 8. Left panel: The probability density functions (PDFs) of the *intrinsic* FRB population versus redshift, for PL, SFR and delayed SFR models with three delay times. The redshift range $[0, 1.5]$ is used in our simulation. For information, we also show the region $[1.5, 2.5]$, gray shaded, such that the shift of the SFR peak is visible between the models. Right: The simulated *observed* FRB population PDFs against redshift, for the same models. The mean redshift $\langle z \rangle$ for the different models are marked by the dashed vertical lines. An unfilled zoomed-in view of the redshift range $[0, 0.2]$ is also shown.

Models	Statistics				
	$A^2_{S/N}$	$A^2_{w_{\text{eff}}}$	A^2_{DM}	A^2_{total}	BIC
PL	1.6	1.6	-0.2	3.0	60.9
SFR	1.1	-0.3	-0.1	0.7	48.4
Delayed SFR - 0.1 Gyr	1.3	-0.6	-0.8	0.2	46.8
Delayed SFR - 0.5 Gyr	1.1	-0.6	-0.6	0.2	46.8
Delayed SFR - 1 Gyr	1.4	-0.6	-0.8	-0.1	46.9

Table 2. A summary of the A-D statistic and BIC for different models. These values are averaged from 50 realizations using best-fitting parameters for each model. The BIC shows no evidence in favor of the delayed SFR models over SFR model, and strong evidence of over the PL model.

5.1. The number of FRBs in the local Universe

Using `frbpoppy` and the CHIME/FRB Catalog 1 we can establish of how many FRBs are born and go off per day in our local Universe, which we define to be up to $z=1$. We present this fiducial number here to provide a best estimate based on our simulations. The number depends on the model parameters (as discussed above) and readers are invited to run their own simulations if desired. We use our best-fit no-delay SFR model (with spectral index -1.5 , luminosity index -1.58 , and minimum luminosity $10^{41} \text{ erg s}^{-1}$). We input the CHIME/FRB rate of $820 \pm 60 \text{ (stat.)}_{-200}^{+220} \text{ (syst.) sky}^{-1} \text{ day}^{-1}$ for fluence $> 5 \text{ Jy ms}$, scattering time $< 10 \text{ ms}$ at 600 MHz, and $\text{DM} > 100 \text{ pc cm}^{-3}$.

From these we determine the rate of non-repeating FRBs that happen in the $z < 1$ volume: $10^{8.3 \pm 0.4} \text{ day}^{-1}$. In other words, from us out to $z=1$, between $4 \pm 3 \times 10^3$ FRBs go off every second.

5.2. How FRB formation trails the SFR

In our models, the scenario where FRBs follow the delayed SFR is slightly favored over no delay (Table 1). This agrees with the findings of James et al. (2022b), but is in contrast with Zhang & Zhang (2022). As all SFR-based models are strongly favored over PL models, our results indicate that FRB emitters must be the direct descendants of a stellar population. Source classes such as neutron stars, magnetars (CHIME/FRB Collaboration et al. 2020a; Bochenek et al. 2020), and stellar mass black holes fit this description. Coalescing neutron stars generally take a much longer time to merge (e.g., Pol et al. 2019). Still we know of one FRB in an environment long devoid of star formation:

FRB 20200120E, in a globular cluster of M81 (Bhardwaj et al. 2021; Kirsten et al. 2022). That example means we should consider the possibility there is some fraction of FRBs that does exhibit a delay. Proposed models for FRB 20200120E are induced collapse of a white dwarf through accretion (accretion-induced collapse, AIC), or from the merger of two white dwarfs (merger-induced collapse, MIC). In such models, the white dwarf inspiral is driven through gravitational-wave energy losses originally, and finally through mass transfer. Kremer et al. (2023) find that after 9 Gyr, the approximate age of the M81 globular cluster, white-dwarf mergers continue to occur, forming young neutron star that are the FRB emitters; although the relatively low rate requires a long, 10^5 yr active emitter lifetime. Whatever the model, FRB 20200120E exists and its formation trails the SFR by billions of years. How many such FRBs can be mixed in with a general population of FRBs that *does* closely follow the SFR? To investigate this we created a hybrid intrinsic population, of which 90% of the FRBs follow SFR immediately, while the other 10% are deferred by 1 Gyr. Hence, these FRBs have a mean delay time of 0.1 Gyr. Although the hybrid population has more low- z events, it hardly deviates from the purely 0.1 Gyr delay mode in our results. We conclude that the average delay time is the most important parameter. As our models favor short delay times, the fraction of deferred FRBs cannot be large.

Other ways to elucidate the connections between FRBs and star formation exist in principle. From the locations of 8 FRBs within their host, Mannings et al. (2021) find no convincing evidence that FRBs strictly follow star-formation, nor that they require a delay; and an FRB survey with LOFAR in star burst galaxy M82 found no bursts (Mikhailov & van Leeuwen 2016).

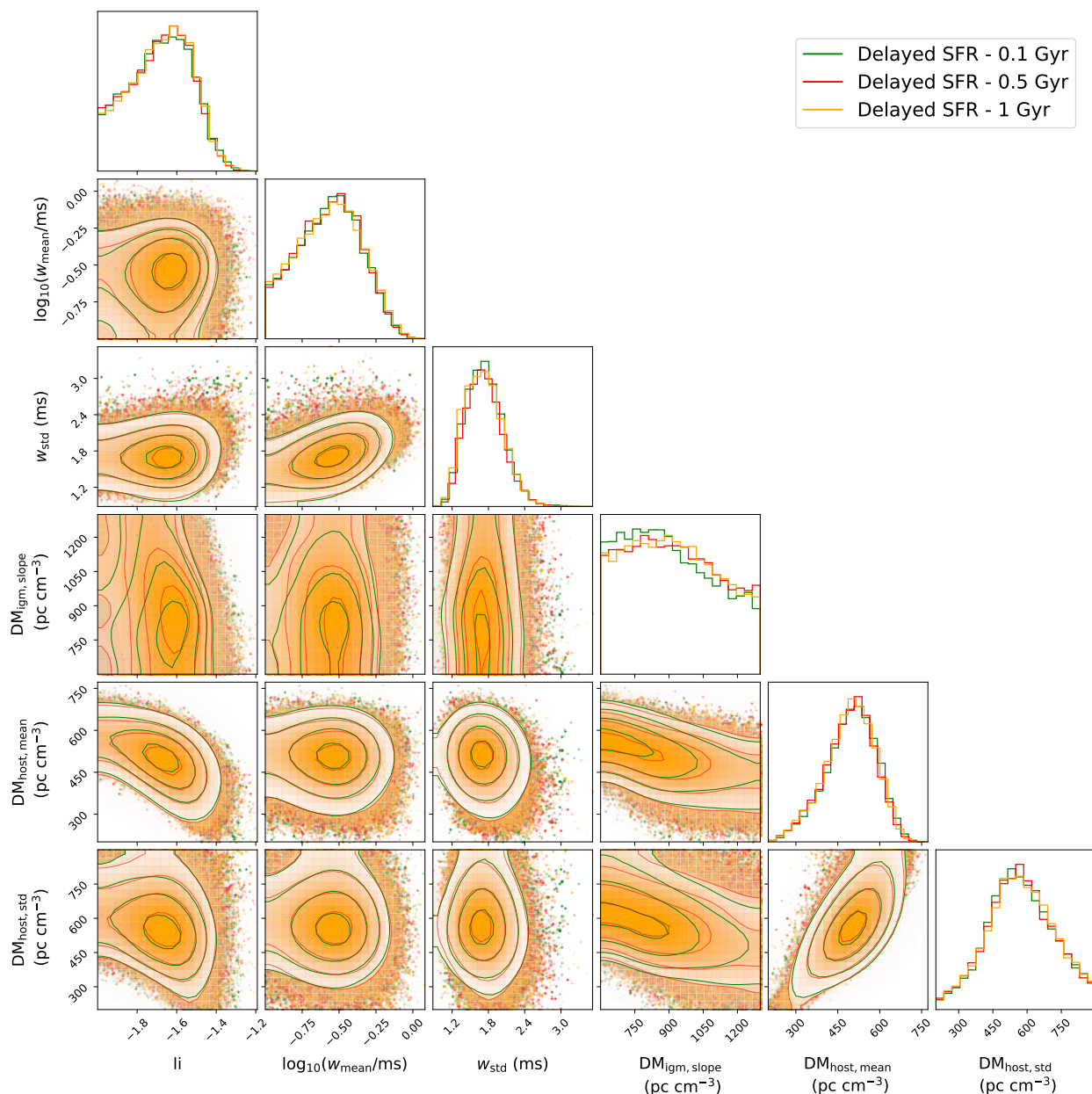


Fig. 9. The confidence contours and marginalized likelihood distributions for three delayed SFR model (0.1, 0.5, 1.0 Gyr).

5.3. Side-lobe detection fraction

As discussed in Sect. 2.3.1, CHIME effectively performs a deep (main-lobe) and shallow (side-lobe) survey simultaneously. The side-lobe plateau incorporated in our simulations ranges over $\pm 15^\circ$ (East-West) and is thus significantly larger than the main-lobe, as that roughly spans $\pm 2^\circ$ (Fig. 3). On average, this side-lobe region under consideration is over a $100\times$ less sensitive than the peak sensitivity. Any FRBs detected there must be very bright; and other such bright FRBs must then also occur in the main-lobe, where they are seen as high-S/N bursts (see, also, Lin et al. 2023). The 3 side-lobe FRBs reported in CHIME/FRB Catalog 1 have S/Ns of 21, 20, and 13. We would thus also expect $\sim 1\%$ of main-lobe FRBs to have S/Ns $100\times$ higher, of 10^3 to 10^4 . And yet, the highest S/N detected in CHIME/FRB Catalog 1 is only 132.

We thus conclude that the CHIME/FRB pipeline missed a significant number of very bright FRBs. We would expect these

bursts to be relatively nearby and hence, display low DM. Merryfield et al. (2023) mention that the CHIME/FRB pipeline has a bias against such bright, low-DM FRBs through clipping during initial cleaning of RFI radio frequency interference at the L1 stage. The detection efficiency suggested that $\sim 7\%$ of detectable injections above an S/N of 9 were mislabelled as RFI (Merryfield et al. 2023). Efforts to improve the CHIME/FRB pipeline in this regard could be worth while. Bright, low-DM FRBs will be sources of great interest, for exact localisation within the host galaxy, multi-frequency follow-up and for progenitor studies that help describe FRB formation.

Our simulations actually suggests that $\sim 2\%$ of the FRBs should have been brighter than the maximum observed S/N in Catalog 1 (discussed in more detail in the following Sections; visible in Fig. 12). Local sources, originating from $z < 0.1$, constitute $\sim 60\%$ of those bright events. Therefore, a rough estimate suggests that CHIME/FRB may so-far have missed of order 5 bursts ($\sim 1\%$ of its Catalog 1 size of ~ 500 ; CHIME/FRB Collab-

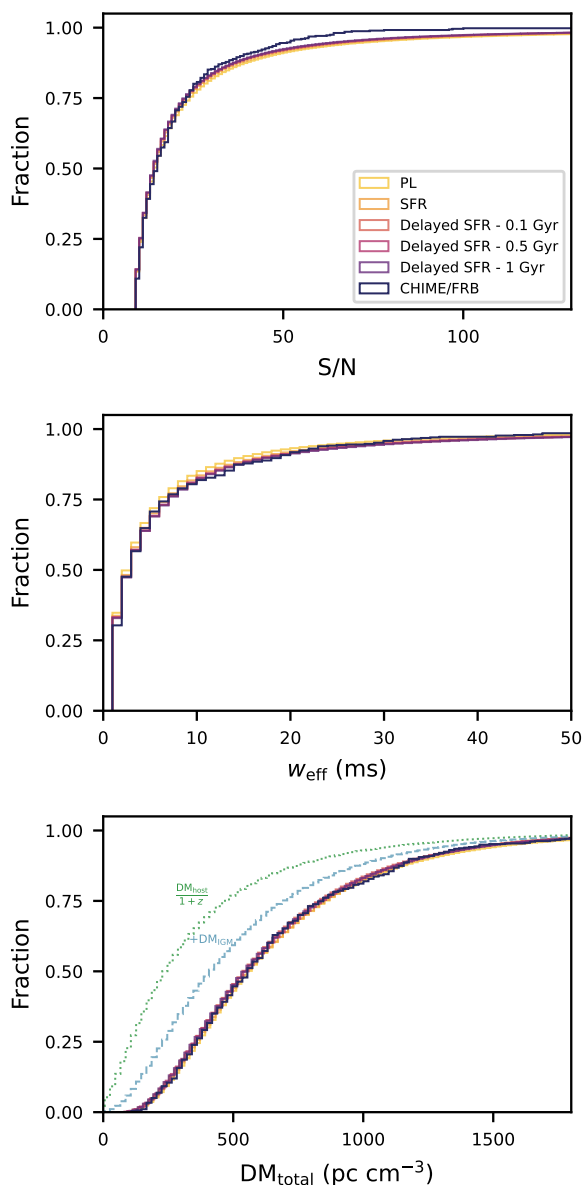


Fig. 10. A comparison of cumulative distributions for simulated populations with best-fitting parameters and the CHIME/FRB Catalog 1 one-off FRBs. The S/N, w_{eff} and DM_{total} are shown in upper, middle and lower panels respectively. The population coloring is the same in all subplots. In the DM plot we also show the cumulative contributions of $\text{DM}_{\text{host}}/(1+z)$, and of the additional DM_{IGM} , for the delayed SFR model with 0.1 Gyr. These show how, for the lower-DM half of the population, these two components contribute roughly equally to the DM_{total} ; while for the higher-DM half, the host contribution dominates.

oration et al. 2021) that are local, bright FRBs – these remain to be discovered.

Our simulations indicate that equally bright FRB sources must next also be detectable in the side-lobes more often than the reported $< 1\%$ (3 out of 474). We expect a side-lobe detection fraction of $\sim 1.8\%$ in the delayed SFR models, $\sim 2.2\%$ in the straight SFR model, and $\sim 2.6\%$ in the PL model. The location of these detections are shown in Fig. 11. All the models considered here thus predict more side-lobe FRBs than Catalog 1 contains.

The alternative explanation for both absences is that there is some intrinsic fluence cut off, which prevents side-lobe detections and high-S/N main-lobe detection alike. The fluence, how-

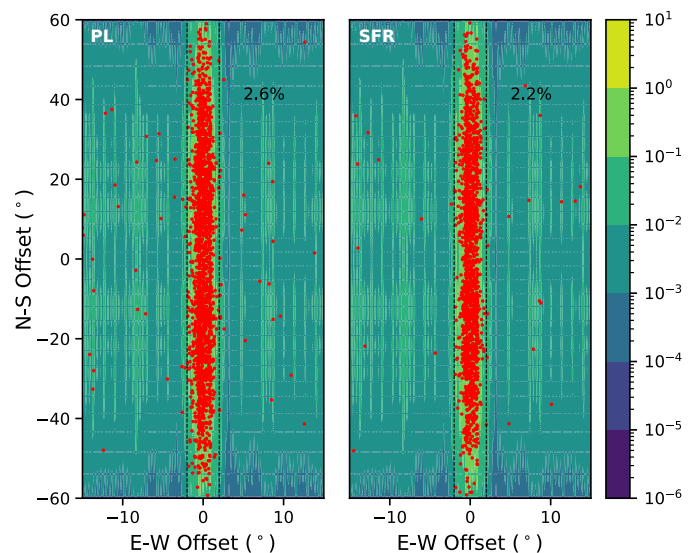


Fig. 11. The detection locations of simulated FRBs in the CHIME beam map (at 600 MHz). The left and right panels are results of the PL and SFR number density model respectively. The vertical dashed lines mark the chosen boundary ($\pm 2.0^\circ$) of the main-lobe. Side-lobe detections account for $\sim 2.6\%$ and $\sim 2.2\%$ in the PL and SFR models respectively, based on the average of 50 realizations. The beam intensity is normalized as in Fig. 3.

ever, is a value that is only defined at the observer location. As it is determined by a combination of the distance to the source and its luminosity, which are different for every FRB, the existence of such a cutoff seems very unlikely. The more likely explanation appears to be that there is a bias against high-S/N detections, and that some side-lobe detections go unrecognized as such.

5.4. The CHIME sensitivity and its influence on the S/N and fluence distribution

As introduced in Sect. 2.3.2, the initially predicted CHIME gain $G = 1.4 \text{ K Jy}^{-1}$, system temperature $T_{\text{sys}} = 50 \text{ K}$ and degradation factor $\beta = 1.2$ suggested in CHIME/FRB Collaboration et al. (2018) and used in Gardenier et al. (2019) were found by the subsequent system study (Merryfield et al. 2023) to overestimate the CHIME/FRB sensitivity. Therefore, in this work, we adopt $G = 1.0 \text{ K Jy}^{-1}$, $T_{\text{sys}} = 55 \text{ K}$, and $\beta = 1.6$ to agree with that study. These three parameters are most informatively combined when expressed as an effective system equivalent flux density $\text{SEFD}_{\text{eff}} = T_{\text{sys}}\beta/G$ (see Eq. 10). Thus, while frbpoppy previously assumed $\text{SEFD}_{\text{eff}} = 45 \text{ Jy}$, we now use $\text{SEFD}_{\text{eff}} = 90 \text{ Jy}$. This more realistic value underlies all above-mentioned results.

We here discuss the influence of this change on some of our metrics, especially on the agreement of the observed and simulated S/N distributions (see, e.g., Eq. 12). In earlier sections, we have displayed these distributions as CDFs (e.g., Fig. 10). In this current discussion, we display similar data but now as distributions of cumulative number $N(>x)$ versus x . Observed sets of bursts, for both one-offs and repeaters, are commonly visualized this way for either the number $N(>x)$ or rate $R(>x)$, against S/N, fluence or luminosity as variable x (e.g., CHIME/FRB Collaboration et al. 2020b; Pastor-Marazuela et al. 2024).

We find that the change in SEFD_{eff} has no influence on the slope and GoF of the S/N distribution. This indicates that despite selection effects and different telescope sensitivities, the S/N distribution remains scale-invariant. In Fig. 12 (left) this

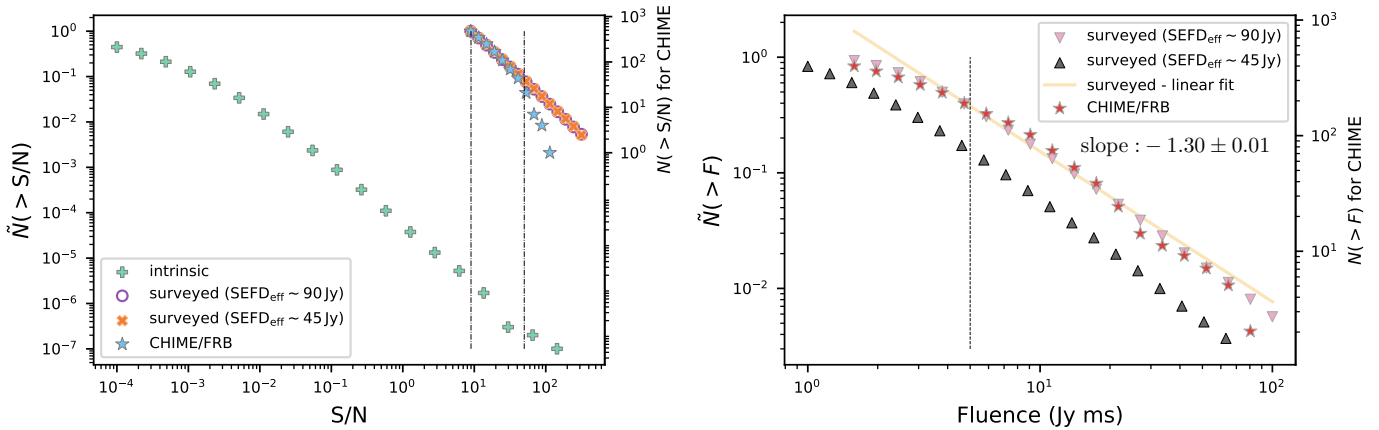


Fig. 12. The cumulative distribution of the S/Ns and fluences of FRBs in the SFR model. On the right ordinates, the number N detectable/detected for CHIME. On the left ordinate, the fraction of this number over the total, $\tilde{N} = N/N_{\text{total}}$. *Left panel:* Plot of $N(>S/N)$ versus S/N . The two simulated populations, surveyed with different SEFD_{eff} , are shown with cross and circle markers, while the CHIME/FRB Catalog 1 is represented using star markers. The S/N “underlying” distribution is generated using a threshold below the minimum range of this plot. The intrinsic and both surveyed populations have the same slope, indicating a scale-invariant feature despite selection effects and different telescope sensitivity. The vertical dash-dotted lines mark the S/N for the CHIME/FRB S/N threshold and for the start of the high- S/N deviation from our surveyed populations, respectively. *Right panel:* $N(>F)$ - F plot. The surveyed population with different SEFD_{eff} and CHIME/FRB Catalog 1 are shown in triangle down, triangle up and star markers respectively; the linear fit to surveyed population ($\text{SEFD}_{\text{eff}} \sim 90$ Jy) has a slope -1.30 ± 0.01 . The vertical dashed line at 5 Jy ms marks the lower bound used in our comparison of fluence distributions.

is visible from the identical sets of points for the two surveyed sets. In the same Figure, the scale invariance is even more visible in the underlying S/N distribution (where we use $\text{SEFD}_{\text{eff}} \sim 90$ Jy but no lower limit). The intrinsic population keeps a constant slope across almost the entire S/N range, thus validating the scale invariance of the S/N distribution. For comparison, the CHIME/FRB Catalog 1 sample is shown with star markers. It diverges from our trend from $S/N > 50$, suggesting CHIME missed high S/N events.

While the S/N distribution cannot distinguish between the old SEFD_{eff} and the new, the fluence distribution can. As shown in Fig. 12 (right) the surveyed population with the updated $G = 1.0 \text{ K Jy}^{-1}$, $\beta = 1.6$ and $T_{\text{sys}} = 55 \text{ K}$ matches perfectly with the CHIME one-offs, while the survey using the preliminary, more sensitive value has significant discrepancies. For example, 38% of FRBs in the CHIME/FRB Catalog 1 have fluences > 5 Jy ms (the dashed line in the right panel of Fig. 12). The new SEFD_{eff} recreates this very well (36%) where the old one could not (17%). We are thus confident the degradation factor is made up of actually occurring (and normal) imperfections or inefficiencies in the survey, related to e.g. corrections for the beam intensities, or pipelines.

5.5. Luminosity

In the current study, the lower and upper boundary of the luminosity are no longer free parameters as these are hard to constrain in the MCMC simulation. However, the L_{max} can influence the maximum S/N in the surveyed population. Continuing the discussion from the previous subsections, the S/N threshold of CHIME/FRB Catalog 1 is 9 and the current maximum S/N is 132, which means the S/N range is smaller than two orders of magnitude. However, our luminosity range spans five orders of magnitude (10^{41} to $10^{46} \text{ erg s}^{-1}$). Under the power-law distribution of luminosity, we would have expected 2%, i.e., of order 10, of the discovered FRBs to exceed this current maximum detected S/N of 132 (see Fig. 10, top panel). Of the detected sample, 0.1%

of FRBs should have $S/Ns > 1000$; Given that the CHIME/FRB Catalog 1 contains ~ 500 FRBs, the non-detection of such a burst is not constraining.

An exponential cutoff power distribution or smaller L_{max} may result in a smaller maximum S/N in the simulated sample, although the proximity of the sources is unaffected, which is arguable more influential for this maximum S/N . We thus still expect that many large- S/N FRBs will be observed when the sample size grows. The maximum S/N can provide important clue on the luminosity distribution (e.g., a power-law or cutoff power-law, the L_{max} or L_{cutoff}).

Below we compare our results for the best-fit FRB luminosity models to other observational and theoretical results. While we discuss these, it is important reiterate that two different definitions of the power-law index are commonly used, and care should be taken when comparing the results.

The luminosity power-law index li in `frbpoppy` is applied as $dN(L)/d \log L \propto L^{li}$ or $dN(L)/dL \propto L^{li-1}$. Under this definition, integration reproduces li as the index in the cumulative distribution $N(>L) \propto L^{li}$ of the generated population. The other common definition is to report the exponent α from above mentioned $dN(L)/dL \propto L^{\alpha}$, as reported in e.g., CHIME/FRB Collaboration et al. (2020b). Thus, $\alpha = li - 1$. Both are generally negative numbers. So an $li = -1$ is identical to $\alpha = -2$. The index that determines the faint-end slope in the Schechter luminosity function is defined as this same α (Schechter 1976). Our li is this α plus one.

Now, our li could be measured directly as the slope in the log-log plot of $N(>L)$ versus L of the *intrinsic* generated population. Selection effects will, of course, alter this slope for the observed cosmological population of one-off bursts. This is displayed in Fig. 13: from an intrinsic population following $li = -1.58$, few bursts with $L = 10^{43} \text{ erg s}^{-1}$ are detected (the curve flattens toward lower L_{bol}). Brighter sources dominate the detected sample, meaning the population CHIME sees follows the much shallower power-law with index -0.75 ± 0.02 .

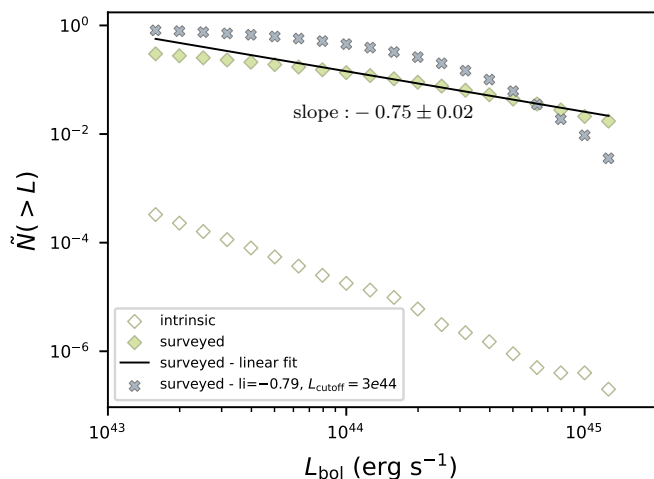


Fig. 13. The fractional cumulative number distribution of FRB luminosities, $\tilde{N}(>L)$ against L , for the best-fit no-delay SFR model. The intrinsic population (hollow diamonds), follows the intrinsic luminosity index -1.58 . The surveyed, detected sample (filled diamonds), however, is modified by the survey selection function, and follows a power-law with index -0.75 ± 0.02 (fit result shown). Grey crosses indicate the surveyed population that would follow from the Luo et al. (2020) Schechter luminosity function.

But for observations of repeater bursts, where fewer such effects occur, this li can be directly compared to the fits (e.g., Fig. 4 in Oostrum et al. 2020 or Fig. 3 in Kirsten et al. 2024).

The preferred value for the luminosity index is $-1.58^{+0.10}_{-0.18}$ (Table 1). That is interesting, because this value based on one-off FRBs agrees with the value found by Oostrum et al. (2020, there called γ) for the repeating FRB 121102, of $-1.7(6)$. It is also consistent with the most complete, high-fluence section of the broken power-law fit to luminosity index for repeating FRB 20180916B reported as -1.4 ± 0.1 in Pastor-Marazuela et al. (2021, there called Γ). This similarity in the pulse energy distribution between one-off and repeating FRBs, something that would be unlikely to occur between completely difference sources classes, corroborates the finding of Gardenier et al. (2021), recently confirmed by James (2023), that the two apparent types both originate from a single population of FRB sources that is actually mostly uniform.

A number of other studies of one-off populations, in contrast, find different values for the luminosity index, but there are important differences and caveats, that we describe below.

The study in Luo et al. (2020), while possibly limited by the small sample size, is similar in set up to `frbpoppy`, albeit without simulating cosmological source evolution. Luo et al. (2020) assumed a Schechter luminosity function and a log-normal intrinsic pulse width distribution, next applying a flux threshold S_{\min} when calculating the joint likelihood function. Their best-fit model based on 46 FRBs from 7 surveys is formed by a Schechter luminosity index α of $-1.79^{+0.3}_{-0.4}$ with cutoff luminosity $\sim 3 \times 10^{44}$ erg s $^{-1}$. This index, which corresponds to our $li = -0.79^{+0.3}_{-0.4}$, governs the faint end of the $N(>L)$ distribution, up to the turn-over luminosity. As FRBs with luminosities below $L = 10^{43}$ erg s $^{-1}$ do not significantly contribute to the observed population (see Fig. 13), the value of the index is not actually constraining. It is the turn-over itself that determines the distribution. To illustrate this behavior Fig. 13 also displays the resulting surveyed population, from a one-off experiment with a Schechter function in `frbpoppy`. Although the distribution is less linear,

the Luo et al. (2020) result is similar to our best model in overall average slope.

Shin et al. (2023) next report a Schechter index α (called the differential power-law index there) of $-1.3^{+0.7}_{-0.4}$, which in our notation corresponds to $li = -0.3^{+0.7}_{-0.4}$ – but for the energy, not the luminosity. That result, too, is based on CHIME/FRB Catalog 1 data. The modeling, however, is more limited. Where `frbpoppy` finds the best model by fitting over the S/N, w_{eff} and DM_{total} distributions, Shin et al. (2023) optimizes for the DM_{total} –Fluence distributions. Fluence may be closely related to the luminosity index we discuss here, but it can only be turned into S/N, the observed quantity, through the pulse width. In Shin et al. (2023) this width is drawn from the inferred observed width distribution, not from an independent source distribution. To ensure understanding of the interplay between pulse width, luminosity and energy, forward modeling of the intrinsic pulse width and any broadening effects from the intervening plasma have been part of `frbpoppy` since inception (Gardenier et al. 2019). One of the main conclusions in Merryfield et al. (2023), too, is that the CHIME S/N is affected much more strongly by the effective burst width than by the DM. As the pulse widths are not explicitly modeled in Shin et al. (2023), the use of a single energy distribution, not separate luminosity and width distributions, is required. A number of inherent selection effects due to width may be absorbed into the energy function. We hence do not think a meaningful discussion of the astrophysics implied by our different luminosity and energy results is possible.

James et al. (2022a) find that the luminosity index dominates the extent to which FRBs are seen from the local universe, as suggested earlier by Macquart & Ekers (2018) – with steeper values indicating more nearby events in the observations. Therefore, the differences in the required li reflect the different FRB z distribution: James et al. (2022a) find $li = -1.09^{+0.14}_{-0.10}$ and in this case, the fraction of FRBs in the observed sample with $z < 0.1$ is $\sim 10\%$; while in our best model, the more negative $li = -1.58$ requires a larger fraction of local FRBs in the surveyed sample, of $\sim 50\%$ below $z = 0.1$.

5.6. Pulse width

The best-fitting values of $w_{\text{int, mean}}$ and $w_{\text{int, std}}$ are similar among different models. The scattering time follows a log-normal distribution, as is visible in Fig. 14 (right panel). We compare our simulation outcomes against the boxcar width (bc width) provided in the CHIME/FRB Catalog 1, which takes integer multiple of the 0.98304 ms time resolution. For FRBs of small intrinsic pulse width w_{int} , the effective pulse width w_{eff} is dominated by t_{scat} , t_{dm} or t_{samp} . Fig. 14 shows that although there are many events with w_{int} below 1 ms, all of the w_{eff} are above 1 ms due to the scattering and instrumental broadening around 600 MHz. Note that for many FRBs, the CHIME/FRB Catalog 1 only provides their t_{scat} upper limits, which may cause a bias in modeling the lower end of w_{int} .

We see here who two opposing selection effects are at play. In contrast to other models, that are energy based (and thus work in units of ergs; see James et al. 2022b), our model is luminosity based (e.g., working in units of erg s $^{-1}$). This prevents simulations in which unphysically large amounts of energy are output per time unit. Some FRBs are as short as 10^{-6} s (see, e.g., Snelders et al. 2023, and note in Fig. 14 that these are indeed created in `frbpoppy`), others as bright as 10^{42} erg (Ryder et al. 2023); allowing a model to combine these would result in luminosities over 10^{48} erg s $^{-1}$. Such a luminosity exceeds the maxi-

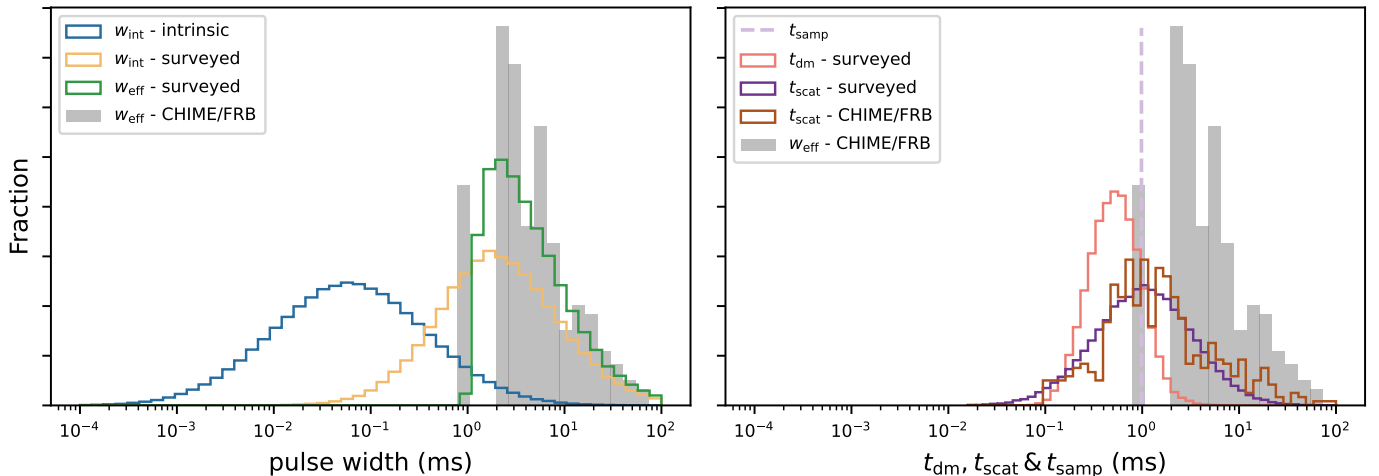


Fig. 14. Left panel: The normalized distribution of intrinsic pulse width w_{int} , for the intrinsic, generated sample and for the surveyed, detected sample, the effective pulse width w_{eff} of this surveyed sample in the simulation, and of the CHIME/FRB Catalog 1 widths. Right panel: The distribution of the simulated normalized t_{dm} and t_{scat} sub-components of the width of the surveyed, detected FRBs; compared to the values from the CHIME/FRB Catalog 1. The sampling time t_{samp} of 0.98304 ms is marked with a dashed line. The population is generated using best-fitting values for the 0.1-Gyr delayed SFR model.

maximum theoretical FRB luminosity under the assumptions of [Lu & Kumar \(2019\)](#), and the maximum spectral luminosities allowed in all but the most extreme parameter combinations in the models of [Cooper & Wijers \(2021\)](#). As described in Sect. 2.2.4, the top end of our luminosity range is based on the brightest *observed* FRBs; as these are harder to miss, this end is likely reasonably complete.

This luminosity basis of our model means wider pulses, on the one hand, have larger fluence (Eq. 8) but on the other are somewhat harder to detect over the noise (Eq. 10). Our treatment of these two selection effects allows us reproduce the CHIME detected widths well.

5.7. Dispersion by the baryonic IGM

The $\text{DM}_{\text{IGM, slope}}$ is relatively poorly constrained in the PL and delayed SFR models, compared to the pure SFR model. This is expected as the fraction of low- z FRBs (e.g., $z < 0.1$) in the former models is higher than in the SFR model. The $\text{DM}_{\text{IGM, slope}}$ appears in the DM_{total} as $\text{DM}_{\text{IGM, slope}}z$. Therefore, to constrain $\text{DM}_{\text{IGM, slope}}$ better, more high redshift FRBs are needed. Within the 1σ uncertainty, the best-fitting values of $\text{DM}_{\text{IGM, slope}}$ are still consistent with the Macquart relation ([Macquart et al. 2019](#); [James et al. 2022a,b](#))

5.8. Host dispersion measures

One of the challenges in understanding the FRB population is that many of its intrinsic properties are tangled into only a small number of observed distributions. One such example is the interplay and overlap of the amount of dispersion caused by the host (DM_{host}), the density of the IGM ($\text{DM}_{\text{IGM, slope}}$), and the distances to the sources. The first two are mainly constrained by the DM_{total} and the w_{eff} distribution; while the distances are constrained by the DM_{total} and the S/N distribution.

There is an anti-correlation between $\text{DM}_{\text{IGM, slope}}$ and DM_{host} in the MCMC contour plot, most obvious in Fig. 7.

In our simulation, we allow a DM_{host} (including the source contribution) to range over a log-normal distribution that is in-

dependent of the redshift. Figure 15 and Table 1 indicate that the best-fitting values of DM_{host} vary only slightly between the different models. In Table 1 we list the *mean* values we find; our *median* DM_{host} in the source rest frame is $\sim 250 \text{ pc cm}^{-3}$ for the SFR model and $\sim 340 \text{ pc cm}^{-3}$ for PL model respectively.

Our values are higher than assumed earlier (including in [GL21](#), who found a constant value of 50 pc cm^{-3} produced an optimal fit). Our new results are also different from e.g. [Shin et al. \(2023\)](#), who find a median DM_{host} of $84^{+69}_{-49} \text{ pc cm}^{-3}$ with a standard deviation of $174^{+319}_{-128} \text{ pc cm}^{-3}$. The difference could, given the anti-correlation mentioned above, be caused by the value $\text{DM}_{\text{IGM, slope}}$ chosen in [Shin et al. \(2023\)](#), where it is not a free parameter. But we infer its value to be around 850 pc cm^{-3} (from their Fig. 10), not that different from our lowest result from the PL model of $\text{DM}_{\text{IGM, slope}} \simeq 780 \text{ pc cm}^{-3}$.

Both [GL21](#) and [Shin et al. \(2023\)](#) find median DM_{host} values lower than the median DM of the known radio pulsars in our own Milky Way (where large selection effects against high-DM pulsar detection are at play, see e.g. [van Leeuwen & Stappers 2010](#)). As FRBs need to escape their host galaxy, which is often massive, it seems surprising it is found to be this low. We find median DM_{host} values of $\sim 300 \text{ pc cm}^{-3}$ though, larger than the median for pulsars. In our results, the total DM is roughly comprised of equal contributions from DM_{host} and DM_{IGM} , but higher values of DM_{total} are generally driven by high host contributions, as visible in Fig. 10 (bottom panel). The median DM for the 6 radio magnetars in our Milky Way, however, is 700 pc cm^{-3} . Our median DM_{host} values are starting to approach this value. In our Milky Way, the line of sight to magnetars cuts through the dense plane. Galaxies containing FRB-emitting magnetars (see [CHIME/FRB Collaboration et al. 2020a](#); [Maan et al. 2022](#)), on the other hand, are generally seen at an angle, with slightly lower DM. We conclude our results support a magnetar origin for FRBs.

From an overall model perspective, the main difference between our work and [Shin et al. \(2023\)](#) is that the latter authors find that the $P_{\text{obs}}(z)$ distribution peaks at ~ 0.36 . None of the number density models that we consider (PL, SFR or delayed SFR) produce a peak at such high redshift. Indeed, the differ-

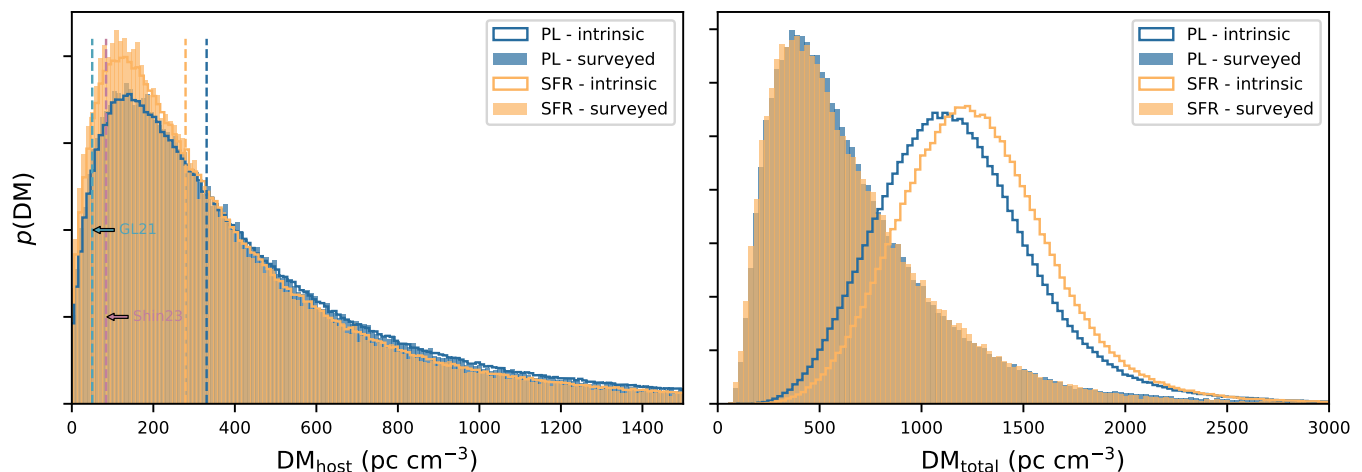


Fig. 15. The normalized distribution of DM_{host} (left) in the source frame, and DM_{total} (right) before (intrinsic) and after (surveyed) detection in our simulation. The median DM_{host} found by GL21, Shin et al. (2023) and this work are indicated with vertical dashed lines. The y axes are in linear scale.

ences in these redshift distribution are strongly correlated with the different DM_{host} between Shin et al. (2023) and our work. If the FRBs are located at higher z , a low DM_{host} is required to reproduce the observed DM curve. We find our values for DM_{host} are reasonable given the knowledge of the known host galaxies (e.g. Bhandari et al. 2022). As `frbpoppy` is open source, we encourage researchers to reproduce these results for themselves.

Our results indicate the selection effects against high-DM hosts are not very strong. This suggests FRBs from the centers of host galaxies are not strongly disfavored compared to those from the outskirts. That is interesting because sources such as magnetars or other young stellar remnants may be found closer to the center, where the dispersion is higher (see, e.g., van Leeuwen et al. 2020 for such a DM model), while globular cluster sources are found more at or beyond the host edge, where DM_{host} is lower.

5.9. Statistics

We use two statistical tools in this study. We employ the GoF to determine the global optimum parameters *within* a model, and we use the BIC method to choose *between* models, and determine which is the best. When deriving the log-likelihood function for the GoF, we have assumed the non-correlation of the three distributions. Although this does not strictly need to be the case, we find that when the minimum of A_{Total}^2 is reached, the $A_{\text{S/N}}^2$, A_{weff}^2 and A_{DM}^2 are all close to minimum as is shown in Table 2. We hence obtain the best-fitting values for all parameters simultaneously.

One could argue that for comparing between models, the Bayes factor is an even better tool, when considering the model complexity. It is, however, not included in the MCMC package `emcee` that is the main focus of the current study. We may consider Bayes factor comparison in future work. The BIC is sufficient for the problem at hand. We produced 50 surveyed populations for each model using the best-fitting parameters, and calculate BICs from the averaged GoFs to reduce the randomness. The results are shown in Table 2. The three delayed SFR models have very close BICs and cannot be distinguished from each other. They show a hint of evidence over the normal SFR model, but strong evidence over the PL model.

5.10. Comparison with other studies

In Table 1 we compare the best-fitting values from our current work against those reported in GL21. In that study, `frbpoppy` could not yet produce formal errors; below we estimate these from the width of the distributions plotted in Fig. 3 of GL21. Our value for α , $-1.58^{+0.09}_{-0.27}$ falls within the Cycle 1 range of the GL21 MC simulation, but in the following runs, their value moved away, to -2.2 . Possibly our full MCMC approach is better able to find the correct global best fit. Our values for the power-law index are consistent with their near-flat li distribution.

Several reasons may account for the differences. In the current work, the parameters s_i , L_{min} and L_{max} are fixed instead of free. Furthermore, in GL21, the observed sample size is smaller, and not uniform in its selection effects. Next, the A-D test we now use for the GoF emphasizes other difference between distributions than the K-S test did. Finally, for finding the global maximum, the current MCMC implementation is a fundamental improvement over the GL21 MC simulation that ran multiple cycles over a number of parameter subsets.

James et al. (2022a,b) studied the z -DM distribution using the ASKAP and Parkes samples (with their code `zDM`⁹), by fitting over a DM-redshift distribution model, a power-law energy distribution and a number density that evolves with modified SFR. They found an estimated maximum FRB energy of $\log_{10}(E_{\text{max}}/\text{erg}) = 41.70^{+0.53}_{-0.06}$ (assuming a 1 GHz bandwidth), a cumulative luminosity index of $-1.09^{+0.14}_{-0.10}$ (discussed previously), an SFR scaling parameter $1.67^{+0.25}_{-0.40}$ and a log-normal distribution of DM_{host} with mean $129^{+66}_{-48} \text{ pc cm}^{-3}$.

Shin et al. (2023) build on James et al. (2022b), but now for CHIME/FRB Catalog 1. They perform a seven-parameters MCMC inference based on the DM-Fluence distribution, in which the likelihood function was evaluated by comparing the counts per bin between the observed and modeled FRB samples. We contrasted their findings to ours in Sect. 5.8, specifically on the DM, the underlying number density input model, and the derived redshift distribution. Note that unlike James et al. (2022b), Shin et al. (2023) appear to not forward model the intrinsic pulse widths, or the subsequent scatter broadening. The authors use

⁹ <https://github.com/FRBs/zdm>

selection-corrected fiducial distributions from the injection system in stead. This pulse width has a large, correlated influence on both the source and the telescope behaviour. It strongly affects the telescope S/N, which is the most important metric for detection; and it has large influence on the emitted burst energy, assuming a given luminosity. Given these unmodeled correlations, [Shin et al. \(2023\)](#) necessarily have to limit their sample to avoid parts of the distribution were these selection effects occur. In the end their comparison is based on 225 bursts. We model more selection effects, incorporate the entire catalog, and fit for more observables: S/N, w_{eff} and DM_{total} .

[Cui et al. \(2022\)](#) selected a sample of 125 burst and report their luminosities follow a log-normal distribution. We, however, find a power-law luminosity function is a good fit. Possibly the selection criteria used in [Cui et al. \(2022\)](#), $S/N > 12$, introduces a bias against low luminosity FRBs and consequently add weight to the log-normal model.

[Bhattacharyya et al. \(2022\)](#) performed a three-parameter MCMC simulation with a 82 one-off burst sample to study the FRB spectral index, luminosity spectral index and mean energy, and [Bhattacharyya et al. \(2023\)](#) next used the CHIME/FRB Catalog 1 to perform a similar study. We have discussed in Sect. 2.2.3 that a survey at a single frequency is incapable of pinning down the spectral index, and allowing it to vary anyway introduces strong covariances in the luminosity function. This is prominent in the results reported in [Bhattacharyya et al. \(2023\)](#). We did not consider a Schechter luminosity function in our MCMC, and thus cannot compare against the cutoff energy and exponent found in [Bhattacharyya et al. \(2022\)](#). As the fitting of the energy distribution in that work does not appear to account for the selection function of the telescope, a meaningful comparison would have been difficult, regardless.

[Chawla et al. \(2022\)](#) studied the dispersion and scattering properties of the FRBs in Catalog 1, through a cosmological population synthesis. They find a DM distribution similar to ours, but their scattering time distribution that extends further into the high end (>10 ms) than our results. Still, our pulse width distribution reproduces the widths seen by CHIME without the need of such a high-end tail. In the left-hand subplot of Fig. 14 this is visible from the agreement between the gray histogram and the green line. In that Figure, the detected simulated pulses (orange) are clearly be part of the large-width tail of the intrinsic distribution (blue). Scattering, next, is a large further addition to the observed pulse width, as visible in the right sub-panel of Fig. 14.

Overall, we find that our results are based on matching more observables than other work and we consider them more robust. The validity of our best models is evidenced by the smaller error budgets we attain. For example, on the luminosity index we produce errors of -0.18 , $+0.10$, significantly better than the -0.4 , $+0.7$ of [Shin et al. \(2023\)](#) or the -0.4 , $+0.3$ of [Luo et al. \(2020\)](#).

5.11. Future work

Since `frbpoppy` now takes account into the selection effects important for CHIME/FRB, logical future steps include inferring the best-fitting populations from the next CHIME/FRB Catalog release. As `frbpoppy` is open source, any interested astronomer can take this on.

Furthermore, a more in-depth and direct comparison of the various populations synthesis codes used in the community (mentioned in the previous Section) would be of great interest if we want to understand code difference, and hence come to a more complete understanding of the actual population. Both

`frbpoppy` and `zDM` ([Prochaska et al. 2023](#)) are open source, and we urge others to publish reproducibly, too.

Once available, such codes could be validated on the same data set as ground truth, with the same metrics. A collaboration that includes one of us started a similar bench mark for public FRB search codes (see [Connor et al. 2020](#); [Melo et al. 2020](#)) with the goal of improving code and furthering open science. A similar comparison of population study codes would be beneficial for validation, improvement and sustainability of the projects involved.

Natural progression of the current results (as mentioned before) would further entail inclusion of CHIME/FRB repeater FRBs, and of the other new surveys with tens of FRB detections.

6. Data and code availability

We provide a number of ways for interested astronomers to use our results.

6.1. Data availability

To get started immediately, one can navigate to the `frbpoppy` quickstart section on Zenodo¹⁰ and download `1_Day_FRB_Sky_on_Earth.txt`. That human and machine readable file contains a simulated 1-day catalog of one-off FRBs, that allows users to access the FRB population without installing the entire `frbpoppy` package. Out of the $10^{8.3}$ FRBs that happen every day between us and $z=1$ (Sect. 5.1), 3.5×10^6 are brighter than 0.01 Jy ms, the best limit in one-off FRB detection currently ([Niu et al. 2021](#)) and in the foreseeable future. The simulated catalog is produced by the perfect telescope in `frbpoppy`, free of selection effects, that observed 4π of sky for 24 hrs, with minimum detectable fluence 0.01 Jy ms, for the best-fit no-delay SFR model.

The catalog lists the coordinates, redshift, distance, width, DM, luminosity, fluence, and other properties for this 1-day snapshot of 3.5×10^6 simulated detected one-off FRBs. Prospective users can integrate the accompanying python reader into their codes if they wish.

6.2. Code availability

Version 2.2.0 of `frbpoppy` is now available through GitHub¹¹. The code continues to support all previous telescopes and population models (including repeating FRBs). This latest version includes the code optimisations and MCMC functionality described in Sect. 3.

7. Conclusions

The updated `frbpoppy` is able to perform an MCMC on the entire CHIME/FRB Catalog 1 and find a single best model for the birth and evolution of the real, underlying FRB population. Where other studies had to curate the input FRBs, our treatment of selection effects allows us to use all one-off FRBs, producing better fits, with smaller errors, than before.

Every Earth day $\sim 2 \times 10^8$ FRBs go off between us and $z=1$, and we make available the mock catalog of the 3.5×10^6 that are potentially detectable. Some of these are nearby and very

¹⁰ <https://doi.org/10.5281/zenodo.11091637> *

¹¹ <https://github.com/TRASAL/frbpoppy> *

* To be made public at paper acceptance

bright, and we have presented evidence that a number of these were missed by CHIME/FRB.

We show that contributions to the DM by the host of several 100s of pc cm^{-3} best describe the observed dispersion distribution, and conclude selection effects against relatively high-DM hosts are not very strong.

We find strong evidence that the FRB population evolves with look-back time, following star formation, with a slight preference for a small delay. We conclude FRBs are produced by the remnants of short-lived stars. The results from our combination of the largest, single-survey data set and the most comprehensive population synthesis code available at the moment thus lend population-based support to the hypothesis that FRBs are created by neutron stars.

Acknowledgements. We thank David Gardenier, Leon Oostrum, and Dany Vohl for interesting discussions and for their support, and Pikky Atri, Kaustubh Rajwade and Ralph Wijers for suggestions that improved this work. This research was supported by the following projects, all financed by the Dutch Research Council (NWO): Vici research project ‘ARGO’ (grant number 639.043.815); CORTEX (NWA.1160.18.316), under the research programme NWA-ORC; plus EINF-3624 and EINF-7739 of the research programme “Computing Time on National Computing Facilities” hosted by SURF.

References

- Amiri, M., Bandura, K., Boskovic, A., et al. 2022, *The Astrophysical Journal*, **932**, 100
- Bates, S. D., Lorimer, D. R., Rane, A., & Swiggum, J. 2014, *MNRAS*, **439**, 2893
- Bhandari, S., Heintz, K. E., Aggarwal, K., et al. 2022, *AJ*, **163**, 69
- Bhardwaj, M., Gaensler, B. M., Kaspi, V. M., et al. 2021, *ApJ*, **910**, L18
- Bhattacharyya, S., Bharadwaj, S., Tiwari, H., & Majumdar, S. 2023, *MNRAS*, **522**, 3349
- Bhattacharyya, S., Tiwari, H., Bharadwaj, S., & Majumdar, S. 2022, *MNRAS: Letters*, **513**, L1
- Bochenek, C. D., Ravi, V., Belov, K. V., et al. 2020, *Nature*, **587**, 59
- Burke-Spolaor, S., Bailes, M., Ekers, R., Macquart, J.-P., & Crawford, F. 2010, *The Astrophysical Journal*, **727**, 18
- Chawla, P., Kaspi, V. M., Ransom, S. M., et al. 2022, *ApJ*, **927**, 35
- CHIME/FRB Collaboration, Amiri, M., Bandura, K., et al. 2018, *ApJ*, **863**, 48
- CHIME/FRB Collaboration, Amiri, M., Bandura, K., et al. 2019, *Nature*, **566**, 230
- CHIME/FRB Collaboration, Andersen, B. C., Bandura, K. M., et al. 2020a, *Nature*, **587**, 54
- CHIME/FRB Collaboration, Amiri, M., Andersen, B. C., et al. 2020b, *Nature*, **582**, 351
- CHIME/FRB Collaboration, Amiri, M., Andersen, B. C., et al. 2021, *ApJS*, **257**, 59
- Connor, L. 2019, *MNRAS*, **487**, 5753
- Connor, L., van Leeuwen, J., Mendrik, A., et al. 2020, An open-source, open-participation competition for Fast Radio Burst detection, <https://github.com/EYRA-Benchmark/frb-benchmark>
- Cooper, A. J. & Wijers, R. A. M. J. 2021, *MNRAS*, **508**, L32
- Cordes, J. M. & Chatterjee, S. 2019, *ARA&A*, **57**, 417
- Cordes, J. M. & Lazio, T. J. W. 2002, *arXiv e-prints, astro*
- Cordes, J. M. & Lazio, T. J. W. 2003, *arXiv e-prints, astro*
- Cui, X.-H., Zhang, C.-M., Li, D., et al. 2022, *Ap&SS*, **367**, 66
- Foreman-Mackey, D., Hogg, D. W., Lang, D., & Goodman, J. 2013, *PASP*, **125**, 306
- Gardenier, D. W. 2019, frbpoppy: Fast radio burst population synthesis in Python, Astrophysics Source Code Library, record ascl:1911.009
- Gardenier, D. W., Connor, L., van Leeuwen, J., Oostrum, L. C., & Petroff, E. 2021, *A&A*, **647**, A30
- Gardenier, D. W. & van Leeuwen, J. 2021, *A&A*, **651**, A63
- Gardenier, D. W., van Leeuwen, J., Connor, L., & Petroff, E. 2019, *A&A*, **632**, A125
- Hu, J.-P. & Wang, F.-Y. 2023, *Universe*, **9**, 94
- James, C. W. 2023, *PASA*, **40**, e057
- James, C. W., Ekers, R. D., Macquart, J. P., Bannister, K. W., & Shannon, R. M. 2019, *MNRAS*, **483**, 1342
- James, C. W., Prochaska, J. X., Macquart, J. P., et al. 2022a, *MNRAS*, **510**, L18
- James, C. W., Prochaska, J. X., Macquart, J. P., et al. 2022b, *MNRAS*, **509**, 4775
- Kirsten, F., Marcote, B., Nimmo, K., et al. 2022, *Nature*, **602**, 585
- Kirsten, F., Ould-Boukattine, O. S., Herrmann, W., et al. 2024, *Nature Astronomy*, **8**, 337
- Kremer, K., Fuller, J., Piro, A. L., & Ransom, S. M. 2023, *MNRAS*, **525**, L22
- Lin, H.-H., Scholz, P., Ng, C., et al. 2023, *arXiv e-prints, arXiv:2307.05262*
- Lorimer, D. R., Bailes, M., McLaughlin, M. A., Narkevic, D. J., & Crawford, F. 2007, *Science*, **318**, 777
- Lorimer, D. R., Karastergiou, A., McLaughlin, M. A., & Johnston, S. 2013, *MNRAS*, **436**, L5
- Lorimer, D. R. & Kramer, M. 2004, Handbook of Pulsar Astronomy, Vol. 4
- Lu, W. & Kumar, P. 2019, *MNRAS*, **483**, L93
- Luo, R., Men, Y., Lee, K., et al. 2020, *MNRAS*, **494**, 665
- Maan, Y., Leeuwen, J. v., Straal, S., & Pastor-Marazuela, I. 2022, The Astronomer’s Telegram, 15697, 1
- Macquart, J. P. & Ekers, R. 2018, *MNRAS*, **480**, 4211
- Macquart, J. P., Shannon, R. M., Bannister, K. W., et al. 2019, *ApJ*, **872**, L19
- Macquart, J. P., Prochaska, J. X., McQuinn, M., et al. 2020, *Nature*, **581**, 391
- Mannings, A. G., Fong, W.-f., Simha, S., et al. 2021, *ApJ*, **917**, 75
- Melo, A., Rubbert, S., Akhmerov, A., et al. 2020, A Collection of Open Science Use Cases, <https://doi.org/10.5281/zenodo.3903257>
- Merryfield, M., Tendulkar, S. P., Shin, K., et al. 2023, *AJ*, **165**, 152
- Mikhailov, K. & van Leeuwen, J. 2016, *A&A*, **593**, A21
- Mo, J.-F., Zhu, W., Wang, Y., Tang, L., & Feng, L.-L. 2023, *MNRAS*, **518**, 539
- Niu, C.-H., Li, D., Luo, R., et al. 2021, *ApJ*, **909**, L8
- Oostrum, L. C., Maan, Y., van Leeuwen, J., et al. 2020, *A&A*, **635**, A61
- Oppermann, N., Connor, L. D., & Pen, U.-L. 2016, *MNRAS*, **461**, 984
- Pastor-Marazuela, I., Connor, L., van Leeuwen, J., et al. 2024, *A&A*, *in prep*
- Petroff, E., Hessels, J. W. T., & Lorimer, D. R. 2019, *A&A Rev.*, **27**, 4
- Petroff, E., Hessels, J. W. T., & Lorimer, D. R. 2022, *A&A Rev.*, **30**, 2
- Petroff, E., Keane, E. F., Barr, E. D., et al. 2015, *MNRAS*, **451**, 3933
- Planck Collaboration, Ade, P. A. R., Aghanim, N., et al. 2016, *A&A*, **594**, A13
- Pol, N., McLaughlin, M., & Lorimer, D. R. 2019, *ApJ*, **870**, 71
- Prochaska, J. X., Baptista, J., & Ghosh, E. M. James, C. W. 2023, FRBs/zdm v0.3, <https://doi.org/10.5281/zenodo.8192369>
- Prochaska, J. X. & Zheng, Y. 2019, *MNRAS*, **485**, 648
- Raftery, A. E. 1995, *Sociological Methodology*, **25**, 111
- Riess, A. G., Yuan, W., Macri, L. M., et al. 2022, *ApJ*, **934**, L7
- Ryder, S. D., Bannister, K. W., Bhandari, S., et al. 2023, *Science*, **382**, 294
- Schechter, P. 1976, *ApJ*, **203**, 297
- Scholz, F. W. & Stephens, M. A. 1987, *Journal of the American Statistical Association*, **918**
- Shannon, R. M., Macquart, J. P., Bannister, K. W., et al. 2018, *Nature*, **562**, 386
- Shin, K., Masui, K. W., Bhardwaj, M., et al. 2023, *ApJ*, **944**, 105
- Snelders, M. P., Nimmo, K., Hessels, J. W. T., et al. 2023, *Nature Astronomy*, **7**, 1486
- Taylor, J. H. & Manchester, R. N. 1977, *ApJ*, **215**, 885
- Thompson, C. & Duncan, R. C. 1995, *MNRAS*, **275**, 255
- Thornton, D., Stappers, B., Bailes, M., et al. 2013, *Science*, **341**, 53
- van Leeuwen, J., Mikhailov, K., Keane, E., et al. 2020, *A&A*, **634**, A3
- van Leeuwen, J. & Stappers, B. W. 2010, *A&A*, **509**, A7
- van Leeuwen, J., Kooistra, E., Oostrum, L., et al. 2023, *A&A*, **672**, A117
- Yamasaki, S. & Totani, T. 2020, *ApJ*, **888**, 105
- Yang, Y.-P., Luo, R., Li, Z., & Zhang, B. 2017, *ApJ*, **839**, L25
- Zhang, B. 2018, *ApJ*, **867**, L21
- Zhang, G. Q., Yu, H., He, J. H., & Wang, F. Y. 2020, *ApJ*, **900**, 170
- Zhang, R. C. & Zhang, B. 2022, *ApJ*, **924**, L14
- Zhang, R. C., Zhang, B., Li, Y., & Lorimer, D. R. 2021, *MNRAS*, **501**, 157